# Multiscale characterisation of diffuse granular failure

Antoinette Tordesillas, Sebastian Pucilowski, Luc Sibille, François Nicot, Félix Darve

# Multiscale characterisation of diffuse granular failure

Antoinette Tordesillas[a]*, Sebastian Pucilowski[a], Luc Sibille[b], François Nicot[c] and Félix Darve[d]

[a]*Department of Mathematics & Statistics, University of Melbourne, Parkville, VIC 3010, Australia;* [b]*ECN, CNRS – Nantes, GeM Laboratory – University of Nantes, France;* [c]*CEMAGREF – Unité ETNA – Grenoble, France;* [d]*3S-R Laboratory – INPG, UJF, CNRS – Grenoble, France*

We study the evolution of structure inside a deforming, cohesionless granular material undergoing failure in the absence of strain localisation –so-called diffuse failure. The spatio-temporal evolution of the basic building blocks for self-organisation (i.e. force chains and minimal contact cycles) reveals direct insights into the structural origins of failure. Irrespective of failure mode, self-organisation is governed by the cooper-ative behaviour of truss-like 3-cycles providing lateral support to column-like force chains. The 3-cycles, which are initially in scarce supply, form a minority subset of the minimal contact cycle bases. At large length-scales (i.e. sample size), these structures are randomly dispersed, and remain as such while their population progressively falls as loading proceeds. Bereft of redundant constraints from the 3-cycles, the force chains are initially just above the isostatic state, a condition that progressively worsens as the sample dilates. This diminishing capacity for redistribution of forces without incurring physical rearrangements of member particles renders the force chains highly prone to buckling. A multiscale analysis of the spatial patterns of force chain buckling reveals no clustering or localisation with respect to the macroscopic scale. Temporal patterns of birth-and-death of 3-cycles and 3-force chains provide unambiguous evidence that significant structural reorganisations among these building blocks drive rheological behaviour at all stages of the loading history. The near-total collapse of all structural building blocks and the spatially random distribution of force chain buckling and 3-cycles hint at a possible signature of diffuse failure.

**Keywords:** granular materials; diffuse failure; force chain buckling; contact cycles; complex networks

## 1. Introduction

What you see in one scale may be different in another – this is a quintessential aspect of complexity which is best exemplified during deformation and failure of granular materials (e.g. soil, rocks, powders, grains, etc.) [1–4]. Complex systems exhibit multiscale patterns of behaviour which are neither perfectly ordered nor perfectly disordered, but somewhere in between [5]. The long-running quest to predict and

*Corresponding author. Email: atordesi@unimelb.edu.au

control the rheological behaviour of granular materials depends crucially on our grasp of the distinctions in their properties, as well as the dominant mesoscopic processes operating across the different spatial and temporal domains. To date, the extant body of knowledge on granular rheology remains predominantly based on macroscopic measurements [3–9]. But this is about to change with the ever increasing volumes of data collected from mesoscopic to microscopic (grain) scale observations in high-resolution experiments and discrete element (DEM) simulations [1,6,10–23]. Here we report on a collaborative study which benefits from data derived from DEM simulations [11,24]. Inspired by the principles originally espoused by Rodney Hill [25] and James Rice [26] for the study of inelastic materials, this investigation forms part of a broader research effort by one of us (AT), which is dedicated towards the development of techniques for material characterisation using the latest advances from the mathematics and statistics of complex systems theory (e.g. [15,22,27,28]). The aim of this effort is to uncover the *essential structural rearrangements* among the material's constituent units (i.e. the grains) in order to understand the root cause and development of failure from inside the material, as well as the evolutionary routes which characterise the different modes of failure in granular materials. This has been made possible by this collaborative investigation into a mode of failure which Félix Darve coined in the late 1990s as 'diffuse failure' [29].

When it comes to the micromechanics of failure in cohesionless granular materials, considerable light has been cast upon the microstructural mechanisms and underpinning dynamics behind the onset of instability and failure via strain-localisation, i.e. shear bands [1,6,14,16,19,22,27,28]. By contrast, knowledge of such for granular failure in the absence of strain-localisation – so-called diffuse failure – is distinctly lacking. A necessary prerequisite for progress is a quantitative definition for diffuse failure. Hence the question that arises is: how does one determine the absence of a pattern of localisation of plastic strain for a given spatial domain? Before a proper characterisation of pattern formation for a complex system can begin, a clear distinction must be made on the length-scale of observation. Granular rheology bears all the hallmarks of complexity, and a past lesson of paramount importance to this study is that complex systems reveal different information at different spatial scales. To date, when the terms 'localised' versus 'diffuse' are used to describe failure modes in geomaterials, the precise point of difference in the spatial distribution and the scale of observation of the failure pattern remains ambiguous [2,4,6,12].

Failure patterns in geomaterials may appear to be localised, dispersed or indiscernible to the naked eye. Those typically associated with localised failure are characterised by zones of plastic strain, concentrated and contiguous in one or several parts of the body: these partition the body into essentially undeforming component masses that can move in rigid body motion relative to each other. However, if we zoom in on the internal structure of such zones of localised plastic strain, even smaller scale failure events (e.g. force chain buckling, vortices) appear to be spread almost regularly throughout the whole band [1,12,15,16,27,28,30]. Those patterns associated with diffuse failure vary in appearance. Some present themselves during failure in rocks and soil as a network of fissures or cracks dispersed everywhere, each of varying characteristic lengths over the small spatial scales, but when viewed at the macroscopic scale, the network as a whole extends

homogeneously throughout the material [3,9]. In other cases, patterns are manifestly absent during failure [3,6–8,24,31–39]: an example is liquefaction, a failure triggered by ground shaking due to an earthquake in moderately dense to loose saturated sand [4,9]. Thus, the evident presence or absence of a particular form of pattern depends crucially on the spatial resolution of observation. From all accounts, the distinction in the spatial pattern of the failure modes in the existing literature appears to be with respect to the macroscopic scale. The challenge, however, lies in the fact that inside the deforming granular material, especially during failure when intense kinematical activity among the constituent grains prevails, a plethora of patterns emerge across the great multitude of mesoscales, right down to the scale of individual grains.

Discrete element simulations in two and three dimensions, and experiments from two-dimensional photoelastic disc assemblies, corroborate Oda and co-worker's hypothesis that shear bands are a manifestation of the localisation of force chain buckling in dense granular materials [1,16,19–21,27,28,40–43]. Kinematical activity at the grain scale, measured using digital image correlation [6,12–15,21] and X-ray microtomography [14,17,18] for various types of sand, also suggests the presence of force chain buckling being confined to the shear band. Accordingly, in this study, we distinguish *localised* versus *diffuse* failure with respect to the spatial distribution of force chain buckling events. That is, we classify a specimen as having undergone diffuse failure if the mesoscopic mechanism of force chain buckling can be demonstrated to be indistinguishable from a random spatial distribution (e.g. homogenous Poisson distribution), when analysed at the macroscopic or spatial scale of the sample. This definition is, of course, predicated on the existence of force chain buckling during failure. Indeed one of the immediate objectives of this study is to determine whether or not force chain buckling is the underpinning mechanism for failure in the specimens in question, claimed to have undergone diffuse failure [10]. The class of granular materials of interest in this study comprises those for which: (i) particle kinematics govern rheology; and (ii) where the solid packing fraction is such that force transmission is facilitated by a percolating network of major load-bearing particles responsible for the deviator stress, amidst and supported by weaker particles for stability [44,45]. Knowledge of the commonalities and differences in the micro- and meso-structural evolution between specimens in this class, undergoing either localised or diffuse failure, is of fundamental as well as practical importance.

On the fundamental side, there remains a multitude of as yet unanswered questions on the precise spatio-temporal origins of failure encountered in granular materials for which grain kinematics governs deformation and flow [2,4,9]. Such questions include: what factors in the boundary conditions and in the initial state of the material favour a localised versus a diffuse mode of failure? What loading conditions (if any) might trigger a switch in the material's response from one of localised to diffuse or vice versa? What are the commonalities and differences in the structural building blocks for self-organisation and their evolution in these two modes of failure?

On the practical side, a comprehensive knowledge of the micromechanics of all modes of granular failure is needed to develop robust predictive continuum models [3]. The phenomenological elasto-plastic constitutive relations being employed today to simulate diffuse failure [46,47] rely on such knowledge for advancement. For example, *in situ* landslides have been simulated using the finite element method

assuming diffuse failure [48], but these continuum mechanics computations have been carried out on the basis of experimental observations at the macroscale. Knowledge of the microstructural evolution underpinning material strength and failure is needed to inform and guide the development of these models, and underpin them on rigorous physical grounds [47,49].

Here we employ novel micromechanical tools for material characterisation to identify fundamental commonalities and differences between localised and diffuse modes in terms of force transmission, with particular attention paid to self-organised load-bearing structures – force chains and supporting contact cycles [19,20,22,27,28,41,42,45,50]. Our immediate objective is five-fold: (i) identify the basic building block structures for self-organisation; (ii) quantitatively characterise their evolution through studies of their populations and lifetimes; (iii) elucidate cooperative behaviour among the load-bearing structures of force chains and their supporting contact cycles; (iv) identify the fundamental mesoscopic failure mechanism underlying macroscopic diffuse failure and (v) characterise the spatial distribution of this failure mechanism along with the supporting contact cycles at multiple length-scales.

The paper is arranged as follows. We first describe the discrete element (DEM) simulations in Section 2. Therein we highlight salient features of the loading programme to provide some insight into the loading conditions to which the two specimens studied here have been subjected, and thereby render more transparent the connection between such conditions and the material's response. The studies discussed in the ensuing Section 3 characterise this connection from the standpoint of the building blocks for self-organisation. Here we also demonstrate quantitatively, through a multiscale spatial pattern analysis, that the specimens are indeed undergoing macroscopic diffuse failure in the sense described above. We conclude in Section 4 with a summary of our key findings and highlight future research directions.

## 2. Discrete numerical simulations

### 2.1. *The discrete element model*

Data for this study came from the three-dimensional discrete element model (DEM) developed and described in detail elsewhere [11,24]. For completeness, however, we briefly describe the salient aspects of this model and the macroscopic rheological behaviour of the two samples to be examined. Following the discrete element method originally introduced by Cundall and Strack [40], each particle of the granular assembly is explicitly described and can interact with neighbouring particles through an interaction contact law, illustrated in Figure 1. The contact law constitutes the only mechanical relation introduced in the model, and defines a relation between the positions of two particles in contact and the contact forces which act on that contact. Motion of particles is then updated each numerical time-step, from the resulting forces and torques acting on each particle, using an explicit time integration scheme of Newton's law. The interparticle interaction (Figure 1b) is modelled in the normal direction to the tangential contact plane by a linear elastic relation, and in the

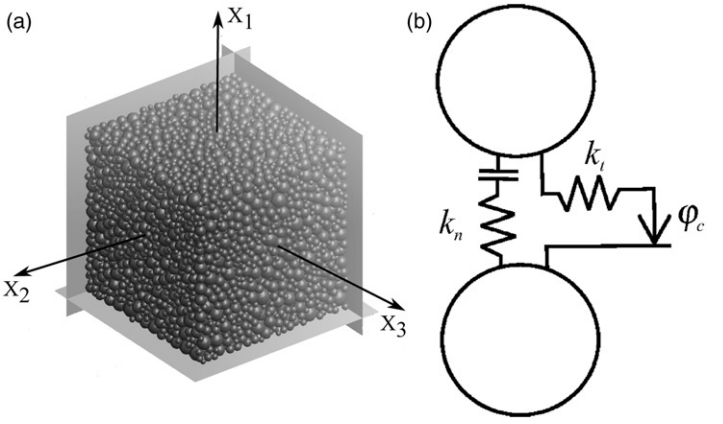


Figure 1. (a) The three-dimensional granular assembly under consideration. (b) Sketch of the intergranular interaction law.

tangential direction by an elastic-perfectly plastic relation. Consequently, the normal and tangential contact forces $F_n$ and $F_t$ are given by:

$$\begin{aligned} F_n &= k_n\, d_n \qquad \text{with} \quad F_n > 0 \qquad \text{(otherwise the contact is lost)} \\ \Delta F_t &= -k_t\, \Delta u_t \quad \text{with} \quad |F_t| \leq F_n \tan(\varphi_c) \end{aligned} \tag{1}$$

where $d_n$ is the overlap between particles and $\Delta u_t$ the incremental tangential relative displacement at the contact point; $k_n$ ($k_n/D_s = 356\,\text{MPa}$) and $k_t$ ($k_t/k_n = 0.42$) are the normal and tangential stiffnesses respectively; finally $\varphi_c = 35\,\text{deg}$ is the intergranular friction angle.

The advantage of this simulation method lies in the fact that only simple physical laws are introduced at the interparticle contact scale. No assumptions are made at the macroscopic scale (i.e. at the scale of the granular assembly). Thus, the emergent macroscopic response of the material is entirely a product of the complex interactions and inelastic structural rearrangements occurring among the constituent units of the system – the grains. Indeed, the popularity of the simple contact laws adopted here, together with the use of idealised particle shapes in DEM simulations, is due to their proven capacity to reproduce the essential defining features and complexities of *real* granular behaviour, including: shear strength dependence on mean pressure, dilatancy, non-associative plastic flows and nonlinearities in the incremental constitutive behaviour (e.g. [11,51–55]), as well as multiple plastic mechanisms at the mesoscopic scale (e.g. shear bands, vortices, force chain buckling, microbands, etc.) [12,15,19,21,22,27,28]. We thus envisage that the grain kinematics in these samples are close to those in real granular materials undergoing diffuse failure, in much the same way that grain kinematics in similarly simple DEM models of localised failure match those observed from real sand and photoelastic disc assemblies which fail in the presence of shear bands [12,15,19,21,22]. Notwithstanding, second-order effects from more complex particle shapes and/or interaction laws are of great interest and the subject of ongoing research (e.g. [43,56]).

The DEM model in [11,24] consists of a cubical shape assembly of approximately 11,000 spherical particles (Figure 1a) of diameter $D_s$ following a continuous size distribution ($D_s^{\max}/D_s^{\min} = 4.75$). At the virgin isotropic state under a confining pressure of 100 kPa, the assembly presents a porosity of 0.382 and a coordination number of 4.54. The macroscopic stress–strain state of the granular assembly is imposed through six frictionless walls, the positions of which are controlled to follow a prescribed loading programme. Since there are no tangential forces in wall–particle contacts, the principal stress and strain directions coincide with the normals to the walls. Each of the principal values of the stresses and strains can be controlled either: (i) directly for strains by adjusting the wall displacements, or (ii) indirectly for stresses, made possible by closed-loop control (since only wall positions or displacements are directly controlled). Consequently, all loading programmes can be implemented with respect to the principal values of the stresses ($\sigma_1$, $\sigma_2$, $\sigma_3$) and/or strains ($\varepsilon_1, \varepsilon_2, \varepsilon_3$). The strain state is determined from the wall positions, whereas the stress state is determined from the wall–particle contact forces.

### 2.2. *Loading programme and macroscopic response*

To render transparent the conditions that led to failure, a brief discussion of the relevant aspects of the loading programmme is warranted (readers are referred to [24] for complete details). The simulations proceed in two phases:

(1) Starting from an isotropic stress–strain state, a strain controlled loading protocol is applied to bring the sample to a mixed limit state, referred to as the 'initial state'. The imposed changes in the strain control parameters are governed by a linear relation, and hence is otherwise referred to as a proportional strain loading path.
(2) From the initial state, a mixed loading programme is imposed to induce failure of the sample. In this programme, a small perturbation of the sample is achieved in two ways, both involving the control of certain strain and stress components.

#### 2.2.1. *Phase 1: from isotropic to a mixed limit state*

In Phase 1, the sample is strain controlled. The three principal strain components ($\varepsilon_1, \varepsilon_2$ and $\varepsilon_3$) are controlled, whereas the three principal stress components ($\sigma_1, \sigma_2$ and $\sigma_3$) constitute the material response to the applied strains. That said, not all strain components are controlled directly; instead a linear combination of some of the strain components are controlled, as it is done for instance to simulate an isochoric compression (where the volumetric strain $\varepsilon_v = \varepsilon_1 + \varepsilon_2 + \varepsilon_3$ is assumed to be constant). In addition, an axisymmetric condition around axis 1 ($\varepsilon_2 = \varepsilon_3$) is assumed throughout this paper. Hence, the isochoric loading condition is here generalised by imposing the axial strain condition $\Delta\varepsilon_1 > 0$ (i.e. the compression) directly, while the following linear combination is imposed between principal strain components [31]:

$$\Delta\varepsilon_3 = -\frac{\Delta\varepsilon_1}{2R} \tag{2}$$

where $R$ is a suitably chosen parameter. Setting $R=1$ recovers the isochoric condition; if $0 < R < 1$, the path is dilatant; and if $R > 1$, the path is contractant. In the case studied here the $R$ value is set to $R=0.825$ corresponding to a moderately dilatant path. These loading programmes, in which the principal strain increments are controlled through a linear relation, are known as proportional strain loading paths [31]. For such loading programmes the control parameters are $\varepsilon_1$ and $\varepsilon_1 + 2R\varepsilon_3$, and the conjugated response parameters with respect to energy are $\sigma_1 - \sigma_3/R$ and $\sigma_3/R$, respectively. Therefore, the computed response to a proportional strain loading path is presented in a $\sigma_1 - \sigma_3/R$ versus $\varepsilon_1$ plot as shown in Figure 2 with the black line for $R=0.825$.

It is also worth keeping in mind that for proportional strain paths, for which the relation $\Delta\varepsilon_1 + 2\ R\Delta\varepsilon_3 = 0$ is imposed, the second-order work $W2$ simplifies to [31]:

$$W2 = \Delta\varepsilon_1\left(\Delta\sigma_1 - \frac{\Delta\sigma_3}{R}\right) + (\Delta\varepsilon_1 + 2R\Delta\varepsilon_3)\frac{\Delta\sigma_3}{R} = \Delta\varepsilon_1\left(\Delta\sigma_1 - \frac{\Delta\sigma_3}{R}\right). \tag{3}$$

Combining the above with the imposed condition $\Delta\varepsilon_1 > 0$, it follows that the sign of the second-order work is the same as the sign of $\Delta\sigma_1 - \Delta\sigma_3/R$. The simulated response curve of $\sigma_1 - \sigma_3/R$ versus $\varepsilon_1$ in Figure 2 presents a peak. At the peak of $\sigma_1 - \sigma_3/R$, the second-order work vanishes and then takes negative values along the decreasing curves.

The mechanical states corresponding to the maximum of $\sigma_1 - \sigma_3/R$ and the ensuing decreasing curves (i.e. corresponding to nil or negative values of $W2$) constitute mixed limit states [31,47]. These mixed limit states can been seen as a generalisation of the classical limit stress states which define the classical plastic failure surface in stress space [31] (represented by the Mohr–Coulomb failure criterion for granular materials). Here the considered limit states are mixed because they cannot be crossed for a proper mixed stress–strain control mode; instead they can be crossed only for a full strain control, as shown in Figure 2, or a full stress

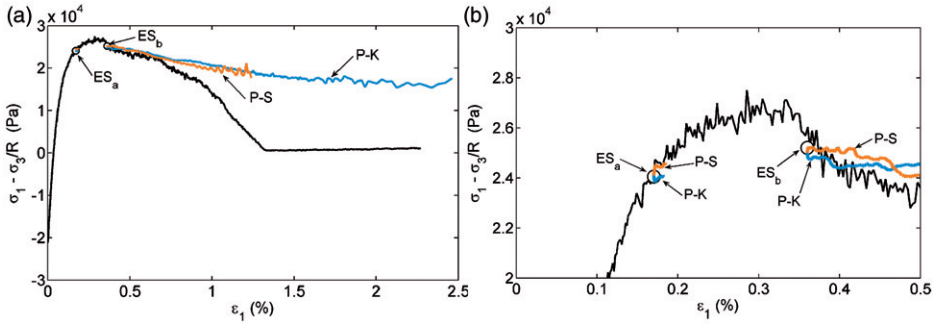


Figure 2. Evolution with axial strain of the generalised stress deviator $\sigma_1 - \sigma_3/R$ for $R=0.825$. In (a) the black line represents the sample response to the first loading applied fully strain controlled. This loading was stopped at state ESa (before the peak of $\sigma_1 - \sigma_3/R$) and at state ESb (after the peak). From states ESa and ESb the loading programme was changed into the loading programmes P-S or P-K. Response paths to these loading programmes are also shown respectively in (a), and with a zoom-in (b).

control for which loading can be carried through until the limit stress state. Consequently, the first phase of the loading programme, wherein the only controlled parameters are the strains, takes the sample to a mixed limit state.

We now consider the stress–strain state denoted as ESb in Figure 2, located slightly after the peak of $\sigma_1 - \sigma_3/R$. This state is a mixed limit state and will constitute the initial state for the two new loading programmes in Phase 2.

#### 2.2.2. *Phase 2: mixed limit state subject to mixed loading protocol*

The second phase imposes a mixed loading protocol, i.e. a small perturbation of the sample, controlling strain and stress components, in order to trigger failure from the mixed limit state. Two types of perturbation are employed and labelled here as P-S and P-K.

2.2.2.1. *Perturbation P-S.* As the response parameter $\sigma_1 - \sigma_3/R$ decreases when the sample is loaded from a mixed limit state, we simply invert the control and response parameters $\varepsilon_1$ and $\sigma_1 - \sigma_3/R$, in order to impose an increase in $\sigma_1 - \sigma_3/R$. Consequently, the loading condition for P-S, imposed at the boundaries of the sample, can be expressed as: $\Delta\varepsilon_1 + 2R\Delta\varepsilon_3 = 0$ and $\Delta\sigma_1 - \Delta\sigma_3/R = 250\,\text{Pa}$. The latter represents around 1% of $\sigma_1 - \sigma_3/R$ at ESb. The response path to the loading programme P-S is displayed in Figure 2, and more detailed time series of strains, stresses and kinetic energy are presented in Figure 3.

2.2.2.2. *Perturbation P-K.* The control parameters are the same as those for loading P-S; however, no change is imposed on the control parameters, i.e. $\Delta\varepsilon_1 + 2R\Delta\varepsilon_3 = 0$ and $\Delta\sigma_1 - \Delta\sigma_3/R = 0$. If such conditions are imposed on the boundaries of the sample, the granular assembly will not evolve and will stay at its initial configuration ESb. However, as shown in [49], the mixed limit state ESb can also be seen as an unsustainable mechanical state, where failure can be triggered by a small perturbation applied to the sample.

Here, we randomly select particles which are not part of the contact network, and then perturb the sample by imposing on these particles a small instantaneous velocity in a random direction (for more details, see [11]). This perturbation, which amounts to an external input of kinetic energy equal to $10^{-4}\,\text{J}$, is small by comparison to the maximum value of kinetic energy (about $10^{-3}\,\text{J}$), computed for the proportional strain loading paths fully strained controlled. The response path to the loading programme P-K applied from state ESb is displayed in Figure 2, and time series are shown in Figure 4. The computed response is very similar to that developed for the programme P-S. There is a sudden dynamic failure of the sample characterised by a total vanishing of stresses, rapid and monotonic strain growth, and a burst of kinetic energy.

Finally, to highlight the importance of the samples' initial state in the analysis to follow, we consider now the state ESa located just before the peak of $\sigma_1 - \sigma_3/R$ in Figure 2. For this state, the second-order work is positive and it should not constitute a mixed limit state (or an unsustainable mechanical state). State ESa is negligibly affected by the application of loading programmes P-S and P-K, as shown

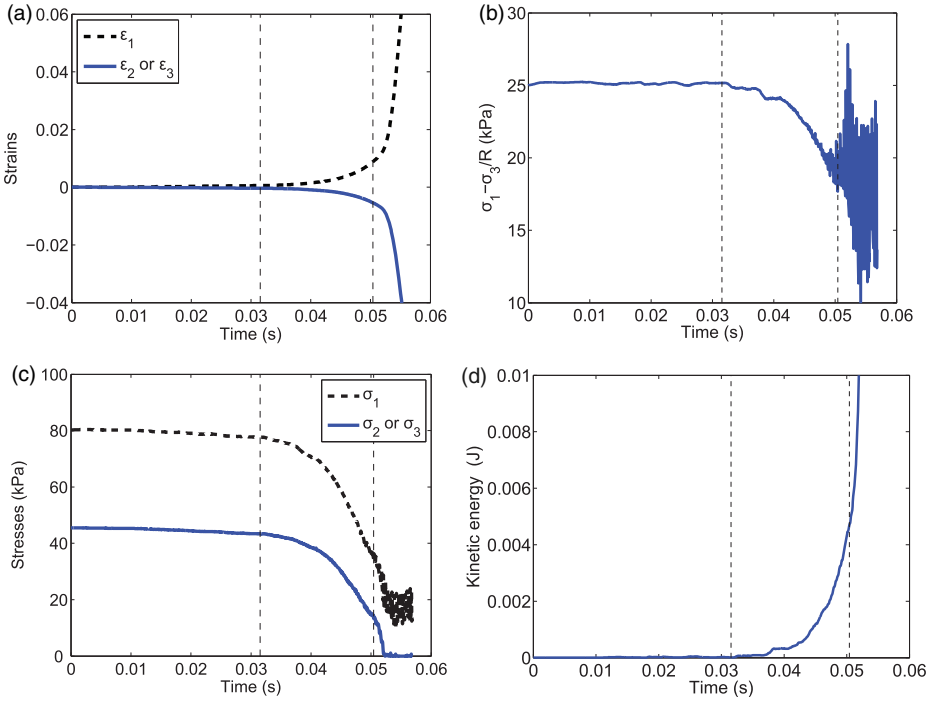


Figure 3. Failure of the granular assembly simulated from the mixed limit state ESb, resulting from the application of the mixed stress–strain loading programme P-S. (a) Axial strains. (b) Generalised stress deviator. (c) Stresses. (d) Global kinetic energy.

by the response paths plotted in Figure 2b. For both programmes, the sample reaches a new equilibrium state close to the initial one (ESa) with a vanishing kinetic energy (not displayed here), and without the development of failure (see [24] for more details). Sample responses resulting from the application of perturbation programmes P-S and P-K from state ESb will be investigated in the subsequent sections the paper. To simplify the designation of each sample response, they will be denoted ESb-S and ESb-K for programmes P-S and P-K, respectively.

## 3. Building blocks for self-organisation

In some respects, the process of self-organisation in granular systems is more directly tractable compared to other well-known complex systems, e.g. telecommunication, social and biological networks [57–62]. Complexity emerges from the interactions of the constituent particles through their interparticle contacts: these contacts can be tracked in real time and the interactions between particles can be quantified through the forces and torques transmitted through these contacts. Other complex networks do not lend themselves so readily to this level of quantitative detail: interactions between two protein molecules or between two human beings or between two computers are difficult to define, let alone measure [57–59,61,62]. We have full

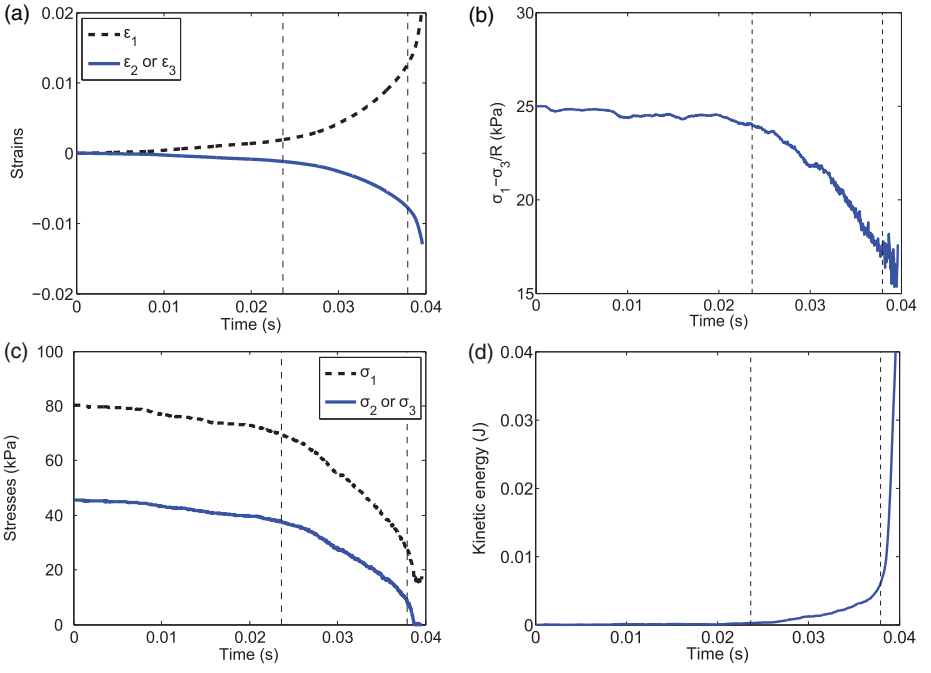


Figure 4. Failure of the granular assembly simulated from the mixed limit state ESb subjected to the loading programme P-K. (a) Axial strains. (b) Generalised stress deviator. (c) Stresses. (d) Global kinetic energy.

information on contacts for the two specimen systems introduced in Section 2, and can thus construct a complex network for each sample at every fixed time in the simulation (or strain state) of its loading history (e.g. [22,27,28,42,43,56]. The nodes or vertices of the network represent the particles in the assembly, while the links or edges connecting the nodes represent physical contacts between the corresponding particles.

Although this abstraction focuses solely on the connectivity of the physical system through interparticle contacts, the influence of system attributes (e.g. interparticle contact laws, particle size and shape distribution, initial packing, etc.) is nevertheless embodied in the evolution of this connectivity – and is thus accounted for in the network analysis, albeit implicitly. That said, the cooperative evolution of basic building blocks for self-organisation in assemblies of particles with more complex shapes (e.g. polyellipsoids in [43]) has been shown to be robust. It is also possible to embed additional information in network representations of granular systems through weighted networks (e.g. using the normal component of the contact force as a link weight as explored recently in [42,43,56]), but this is beyond the scope of the present work. Readers are referred to [27,28,42,43,56,63] for other examples of past characterisation of granular material behaviour, using complex networks constructed from discrete element data. Be mindful though that all of these aforementioned studies focus on systems which fail via strain localisation. Here, for each of ESb-S and ESb-K, we have a series of consecutive complex networks, with

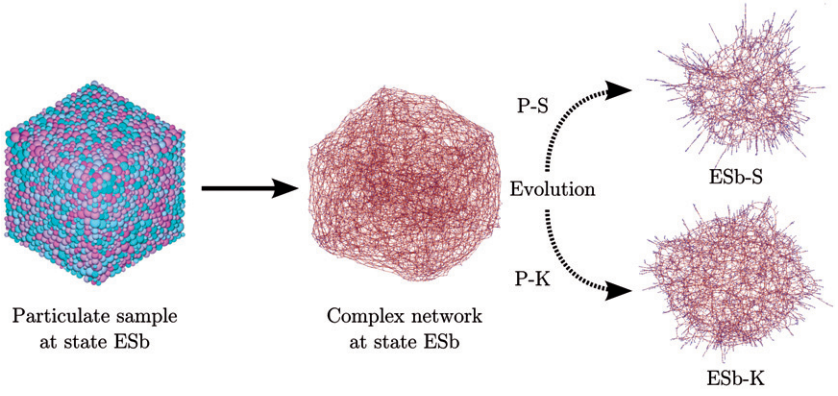


Figure 5. From ESb (left, colours to aid visualisation only), interparticle contacts from discrete element simulations of [11,24] are mapped to an abstract graph or complex network at each time in the simulation (middle). Marked degradation in the physical connectivity of both samples, from the onset of loading ESb to failure, is evident in complex contact networks for samples ESb-S and ESb-K (right).

each network embodying the contact topology at the corresponding state in the loading history. A visual comparison of the initial and final complex networks, shown in Figure 5, already reveals the severe degradation of the physical connectivity in both samples from the onset of loading (ESb) to their respective failure states. Observe the great abundance of particles supported only by one or two contacts at failure, i.e. the 'spokes', which are the particles radiating radially outwards from a central core. By contrast, the contact network at ESb appears to be a relatively homogeneous network of denser connections.

Our first task is to establish the building blocks for self-organisation. This is a necessary prerequisite for any discussion on the properties of structures emerging in the mesoscopic domain (e.g. stability, lifetimes, mode of failure, etc.). The recent studies of dense granular systems which fail by localisation in [19,20,22,27,28,41–43] have identified and characterised the quasi-linear and cyclic building blocks for self-organisation. Here, for the first time, we present the building blocks for two granular samples undergoing diffuse failure, quantify their population and lifetime distributions, and relate these to the particular loading paths described previously in Section 2. Particular attention will be paid to the differences and commonalities in the evolution of structural building blocks for comparison to those found in localised failure systems. We emphasise that we make no claim that the rheological responses we observe and characterise here are universal for that class of dense granular materials undergoing diffuse failure, as defined earlier in Section 1. Rather, the intent here is to start with the particular. That is, we characterise two particular samples in this class, study these systematically, and where differences emerge with respect to those encountered in localised failure, offer some structural insights and plausible clues on why, for certain loading paths, a material may favour a diffuse over a localised mode of failure.

### 3.1. *Linear and cyclic building blocks*

Past studies of dense granular materials undergoing localised failure have shown that force chains and minimal contact cycles may be viewed as the basic building blocks for self-organisation [22,27,28,42,43,56,63]. We begin by identifying these for the two samples ESb-S and ESb-K. Shown in Figure 6 are representative load-bearing quasi-linear structures of $m$-force chains and their supporting cyclic network of contacts, the minimal $n$-cycles, where $m \geq 3$ and $n \geq 3$ are integers representing the number of particles that form the chain or cycle [27]. We refer readers to [27,42,50,58,60–62,64,65] for details of the Complex Network methods and algorithms used to identify force chains and minimal $n$-cycles, derived from the particle-scale information that forms the output data of the DEM simulations described in the previous section. At any given strain state in the simulation, a columnar $m$-force chain is confined by supporting contacts that can be succinctly summarised by the minimal cycle bases of the contact network, i.e. $n$-cycles. Hence each force chain will have its own unique set of minimal cycles of various sizes $n$. In this context, force chains are distinct from $n$-cycles in that force chains are physical structures made up of particles, whereas cycles are made up of contacts with $n$ denoting the number of particles that form the contact cycle. Alternatively, one could consider the physical structure

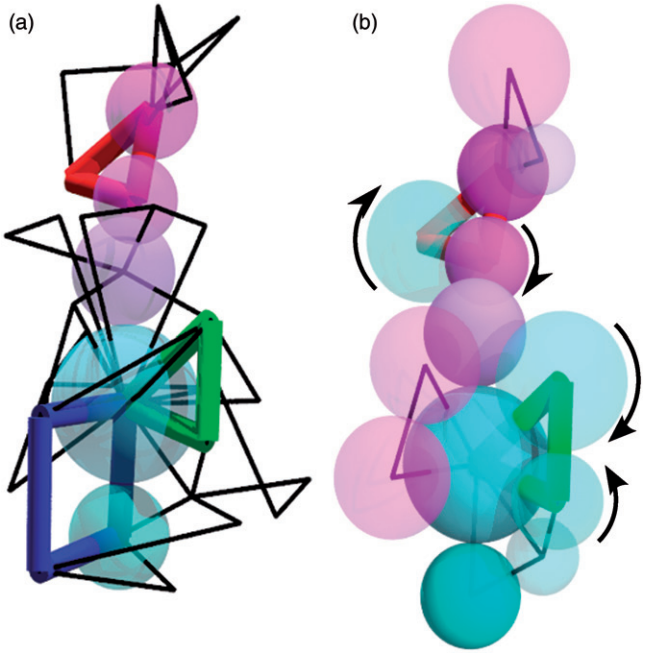


Figure 6. (Colour online) (a) A 5-force chain and its local contact $n$-cycle membership, from the ESb-S sample. This 5-force chain has six 3-cycles, five 4-cycles, seven 5-cycles, two 6-cycles and one 7-cycle. Highlighted are a 4-cycle (blue), and two conformations of 3-cycles, i.e. a 3-cycle with a single edge in common with the force chain (red), and a 3-cycle with a single vertex in common with the force chain (green). (b) Three particles in mutual contact give rise to 3-cycle topologies which frustrate relative rotations of member particles in at least one of the contacts, irrespective of the direction of rotation.

comprising the particles that form the contacts in the $n$-cycle, for the purposes of computing structural properties like stability [22]. The smallest members of the $n$-cycles, i.e. 3-cycles, are special from the standpoint of packing and network connectivity: they are formed from three particles in mutual contact, and thus exemplify a densely packed and tightly connected structure that frustrates relative rotations at contacts [27]. Note that rotations are impeded in groups of particles forming an *odd*-cycle, whereas *even*-cycles allow free rotations (akin to the action of ball bearings) [66,67]. Since particle rotations have long been identified as playing a crucial role in the deformation of granular materials [1,16,19,20,30,40,68] – especially in the failure regime – the *odd*-cycle membership can be reasonably expected to play a key role in the mobilisation of shear strength or resistance to applied loads. Indeed, Arévalo's [63] recent analysis highlights the importance of 3-cycles from the perspective of mechanical rigidity (i.e. transition to jamming) for an isotropically compressed granular packing.

Turning now to the distributions of the populations of $m$-force chains (Figure 7), we find these are qualitatively similar to those for systems that undergo localised failure [22,27,43,50,69]. The number of $m$-force chains, classified according to size or number $m$ of member particles in the force chain, decreases as $m$ grows. The shortest, the 3-force chains, clearly form the majority. From a structural mechanics standpoint, this result is intuitive: like architectural columns, we can expect that with all else equal, a short column would be more stable than a long column and it is reasonable to assume that the more stable force chains would dominate the total force chain population in the system. In a recent study of force chains using structural mechanics techniques [22], the 3-force chains were shown to be the most structurally stable in the system, although the inverse correlation between stability and length weakens for high values of $m$ (typically $m > 5$). This is because the more particles there are in the force chain, the more variations of the contributors to stability become possible (e.g. distribution of the magnitude and topology of lateral forces). We also note that the populations of force chains decrease exponentially with increasing force chain length, with $m > 8$ having negligible populations (not shown); this is consistent with those observed for localised failure [27,42,43,50].

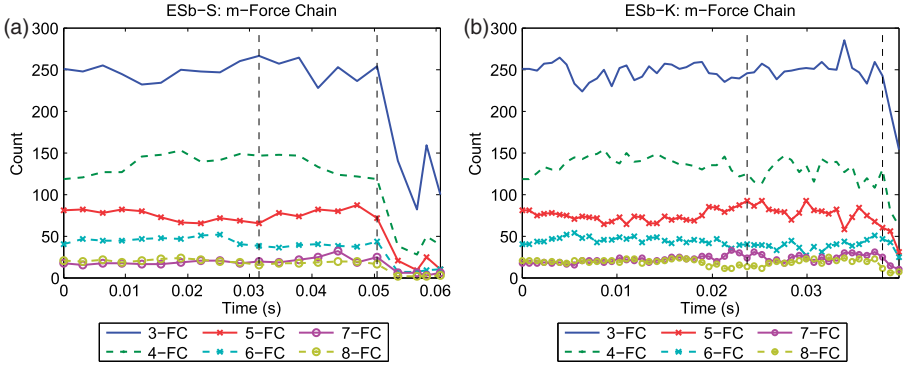


Figure 7. (Colour online) $m$-force chain populations throughout loading for (a) ESb-S, and (b) ESb-K. The shortest 3-force chains form the majority.

More pronounced fluctuations in the evolution of the force chains in sample ESb-K relative to that in ESb-S can be seen from Figure 7. These fluctuations are indicative of structural rearrangements: here the birth of new and death (collapse) of old force chains. Recall from Section 2 that the two samples were perturbed differently from a common initial state ESb. We will return to these aspects of the samples' response in our detailed analysis of birth-and-death processes later in this article.

In contrast to $m$-force chains, the distribution of $n$-cycle populations differs considerably from that for systems undergoing localised failure. Past studies of localised failure show that the $n$-cycle population generally decreases with increasing cycle size $n$, hence 3-cycles comprise the most dominant group [22,27,43]. In Figure 8, we see that the 5-cycles dominate and the 3-cycles now form a minority, never exceeding 16.40% of the total cycle count. Two critical transition times can be observed for sample ESb-S, i.e. at $t = 0.0315$ and $t = 0.0504$. Except for the population of 6-cycles which remain steady initially, we observe an essentially monotonic temporal evolution in the cycle populations that is indicative of the progression of dilatation in the sample: populations of 3-, 4-, 5-cycles decrease, whereas the populations of 7-, 8-cycles increase (higher order cycles have negligible or null populations throughout loading). The degradation of small order cycles amidst growing numbers of large cycles is the prevailing temporal trend for much of the loading history, with the difference being in the rates of change over distinct intervals: the rate starts small in $0.000 \leq t \leq 0.0315$, moderately increasing in $0.0315 \leq t \leq 0.0410$, before a relatively marked increase in $0.0410 \leq t \leq 0.0505$. At just after $t = 0.0505$, there is a sudden drop in all cycle populations corresponding to system collapse. Recalling now the force chain populations in Figure 7, we see that this stage coincides with the failure of most of the load-bearing force chains in the system as is evident in the precipitous drop in their populations. Qualitatively similar trends apply to ESb-K, except that the critical transition times for this sample are around $t = 0.0236$ and $t = 0.0379$. The observation that small low-order cycles cleave and open up to give rise to larger high-order cycles as the sample dilates, prior to total collapse, is consistent with past results on the minimal contact cycle evolution in systems under localised failure [22,27,28,43].

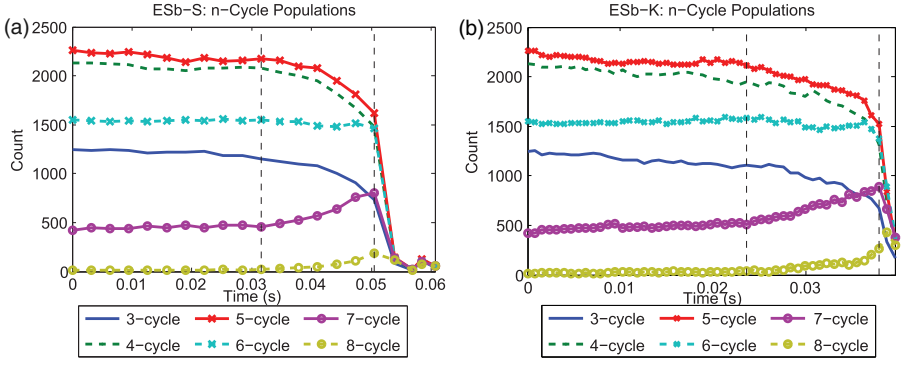


Figure 8. (Colour online) $n$-cycle populations throughout loading for (a) ESb-S, and (b) ESb-K. 3-cycles do not form the majority; instead, higher order 5-cycles dominate.

The above results on the evolution of structural building blocks suggest a partition of the strain history into two regimes, A and B (Table 1). Over regime A, we observe a relatively stable sample response: a near-constant population of major load-bearing $m$-force chains, with only a very mild change in the population of their supporting $n$-cycles. Over regime B, we see a progressive development of instability and failure occurring over two phases. In phase $B_1$, we observe a pronounced increase in the rate of decline (growth) in the population of small (high) order, more densely (loosely) packed 3–5-cycles (7–8-cycles): recall these cycles provide the local support to force chains in the system as shown earlier in Figure 6. Despite the loss of supports, the force chains maintain their numbers and their capacity of support load. This is followed by phase $B_2$, in which *all* supporting cycles irrespective of size collapse, followed immediately by the collapse of the major load-bearing force chains. *Thus for the samples undergoing diffuse failure, the total loss of bulk load-carrying capacity is decidedly due to the precipitous near-total collapse of all the structural building blocks inside these systems*. By contrast, systems which undergo localised failure, maintain *partial* structural integrity throughout the loading history in the sense that a fraction of the population of structural building blocks remains well after the strain-softening regime, when the shear band is fully developed and in its persistent stages [22,27,43,50,69].

In jammed systems [44,70], particles in force chains typically constitute 40–60% of the entire assembly. Here, the percentage of particles forming force chains in both systems is considerably lower, on the order of 25% (Figure 9). This suggests that most of the load is carried by only a small fraction of the granular assembly. This gives rise to two immediate questions: (i) why, under these loading conditions, do these materials 'choose' to allocate the majority of the load to only a small fraction of their respective constituents, and (ii) what makes these 'chosen few' different from the rest? The answer lies in the important 3-cycles. As shown in past studies of samples undergoing localised failure, 3-cycles provide the major load-bearing force chains *dual resistance to buckling* by (i) impeding or frustrating relative particle rotations that are integral to buckling in particulate columns, and by (ii) propping-up the force chains to enforce alignment [27]. Recall that 3-cycles do not form the majority of cycle populations in samples ESb-S and ESb-K (Figure 8).

In Figure 9, we present the percentages of particles in three groups comprising: the 3-cycles, the force chains, and the conjoined (i.e. a particle that is in both a force chain and a 3-cycle as shown, for example, in the largest particle in blue in Figure 6a). For the initial stage ESb, these percentages are a mere 25%, 23%

Table 1. Time intervals of key regimes in ESb-S and ESb-K, inferred from network analysis of structural building blocks. Regime B comprises two consecutive phases, i.e. $B_1$ and $B_2$. The samples undergo global failure in $B_2$, due to the collapse of essentially all the structural building blocks.

| Sample | Regime A | Regime B | |
|---|---|---|---|
| ESb-S | (0.000, 0.0315) | (0.0315, 0.0504) $B_1$ | (0.0504, 0.0606) $B_2$ |
| ESb-K | (0.000, 0.0236) | (0.0236, 0.0379) $B_1$ | (0.0379, 0.0396) $B_2$ |

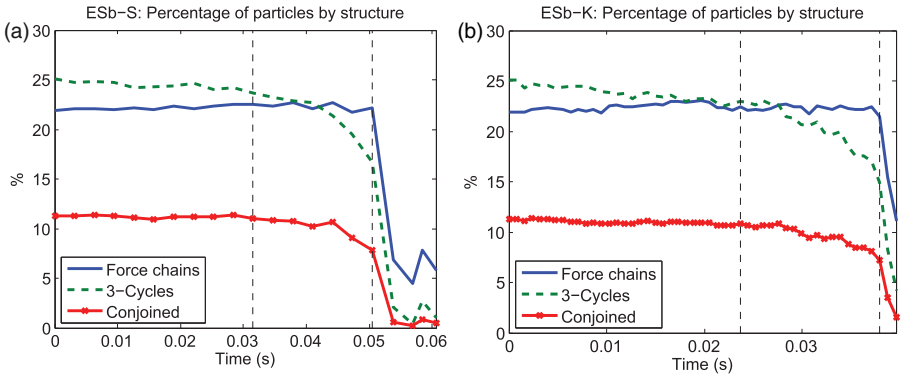


Figure 9. (Colour online) Percentage of particles in force chains and 3-cycles throughout loading for (a) ESb-S, and (b) ESb-K.

and 11% of the total number of particles in the assembly. Those in 3-cycles and in the conjoined set decrease slowly but steadily until sample failure (Figure 9); for comparison, we found above 80% of the total number of particles are initially in 3-cycles in the specimens undergoing localised failure in [27]. This suggests that truss-like 3-cycle supports, critical to the development and maintenance of the load-bearing columnar force chains, are in short supply in these diffuse failure samples. This may therefore explain why there are comparably low numbers of force chains formed in the system at ESb. Note the nearly constant fraction of particles in force chains up until the sample fails (i.e. time 0.0504 (0.0376) in Figure 9 in ESb-S (ESb-K)). During this same interval, there is a corresponding loss of 3-cycles (Figure 8), until some threshold is passed, after which the force chains, along with the 3-cycles, collectively collapse. This, in turn, precipitates the sudden loss of bulk load-carrying capacity of the material over these stages of the simulation, as reported earlier in Section 2.

Indeed, the role of 3-cycles as stabilising agents has been established for a wide range of loading conditions and material properties, albeit for systems undergoing localised failure [22,27]. In these systems, the steady decline in 3-cycles during dilatation compromises the structural stability of force chains, ultimately leaving them prone to collapse by buckling. A similar fate appears to apply to the samples considered here. Overall, this cooperative behaviour between the structural building blocks seems to be a feature that is common to all dense granular materials, irrespective of their mode of failure. We will explore this in more detail later in this article. In the next section, we will examine the extent to which the strain evolution of the building blocks, uncovered in this section, is revealing of the development of failure as observed on the global scale. To achieve this, we will present various indicators of global stability and relate these to the trends in Figures 7–9.

### 3.2. *Connecting mesoscopic to macroscopic structural trends*

The set of necessary and sufficient conditions for a frictional multibody system to be stable remains elusive. The problem is highly nonlinear and the causes of these

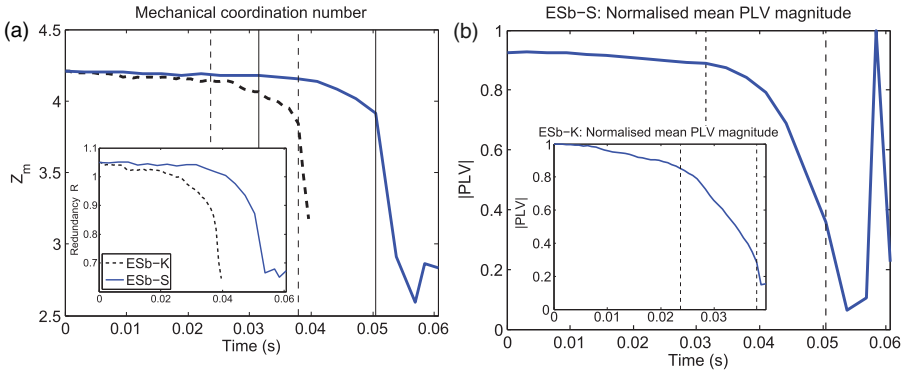


Figure 10. (a) Mechanical coordination number $Z_m$ throughout the loading history for ESb-S and ESb-K. $Z_m = 4$ corresponds to the isostatic coordination number for perfectly rough spheres. (Inset) Redundancy (Equation 5) computed throughout the loading history for ESb-S and ESb-K. $R = 1$ corresponds to the isostatic condition. (b) Global mean value of the minimum eigenvalue (most compressive) of the particle stress tensor, normalised against the peak value reached, throughout the loading history of ESb-S, and (inset) ESb-K.

nonlinearities are too many to track and capture within a rigorous structural mechanical analysis [71]. For granular materials, these difficulties are severely compounded by the vast collective degrees of freedom in the system – the very cause of the complexity that such materials exhibit when placed under load. Until such time as these conditions are established, enquiries into mesoscopic stability must contend with estimates, and great care and caution must be taken in interpreting the results. A way forward is to employ multiple indicators of stability, in conjunction with a detailed analysis of topology, a key contributor to the structural stability of multibody systems. A brief exposition of existing stability measures used in the mechanics and physics communities and their connections to related concepts such as 'jamming transition' and 'isostaticity' is given in [22]. By far the simplest measures are: (i) the average number of contacts per particle (also known as the average coordination number, or average degree in the parlance of complex networks), (ii) the mechanical coordination number $Z_m$ of Thornton and Antony [72], and (iii) the condition for isostaticity as measured by the redundancy parameter $R$. These indicators are interrelated and have been used extensively in studies of packing geometries of jammed configurations [22,23]. In what follows, we focus on the evolution of $Z_m$ and $R$.

The measure of mechanical coordination number $Z_m$ for frictional assemblies is defined as:

$$Z_m = \frac{2N_c - N_1}{N_p - N_0 - N_1}, \tag{4}$$

where $N_c$ is the total numbers of contacts, $N_1$ is the number of particles with one contact, $N_0$ is the number of particles with zero contact, and $N_p$ is the total number of particles [72]. Figure 10a shows that, even prior to failure, both samples are close

to the lower bound for the isostatic coordination number for spheres (i.e. $Z_{iso} = 4$ for perfectly rough spheres and $Z_{iso} = 6$ for frictionless spheres) [22]. To confirm this, we computed the redundancy parameter $R$ [73], defined for the three-dimensional frictional assemblies ESb-S and ESb-K by:

$$R = \frac{3N_{ce} + 2N_{cs}}{6(N_p - N_0 - N_1)}, \tag{5}$$

where $N_{ce}$ is the number of elastic contacts (i.e. contacts where $|F_t| < F_n \tan \varphi_c$) and $N_{cs}$ the number of sliding contacts (i.e. contacts where $|F_t| = F_n \tan \varphi_c$), excluding contacts between particles involved in only one contact. When $R = 1$, the system is marginally stable or isostatic: this state may be thought of as providing a lower bound on all the possible stable states that the system can inhabit. If $R < 1$, the system is under-constrained or hypostatic and this is a sufficient condition for the system to be unstable. It is important to keep in mind, however, that the system being hyperstatic, i.e. $R > 1$, is no guarantee of, and is only a necessary condition for, stability. $R > 1$ does not *per se* imply stability.

The inset in Figure 10a shows, as for the mechanical coordination number, that both samples are only slightly above the isostatic condition in regime A: this is consistent with the relatively small proportion of the important 3-cycles in the total minimal contact cycle bases reported in Figure 8. Keep in mind that 3-cycles bear the highest level of connectivity possible within a close packing arrangement, hence their relative abundance (scarcity) is a direct indicator of structural stability. Indeed, in the recent study in [22], the density of 3-cycles, measured through the complex network property of clustering coefficient [42], shows a very strong positive linear correlation with the redundancy $R$, the mechanical coordination number $Z_m$, and the granular cluster stability $\lambda_0$ developed in [22]. The measure of stability $\lambda_0$, conceived using structural mechanics analysis of a particle cluster of any length-scale, depends not just on the number of contacts but also on other aspects of contact topology (i.e. position and orientation), modes of contacts, material properties, and boundary/loading conditions. Thus, at least qualitatively, we expect the temporal trends we have seen in $R$ and $Z_m$ to reflect the global stability of the sample which, in turn, can be explained by the progressive loss of 3-cycles in these systems.

The results in Figure 10a lend support to the existence of distinct regimes A and B, inferred earlier from the evolution of the structural building blocks in Figures 7–9. That is, regime A is a period over which the material behaviour appears to be relatively stable in the sense that it is in a hyperstatic state (albeit marginal) and has a demonstrated capacity to support load; on the other hand, regime B is a period of instability due to the higher rates of loss of supporting 3-cycles leading to the material becoming under-constrained and, ultimately, unable to support load with the near-total collapse of all the building blocks.

Overall, summarising now the key features from Figures 7–10a, we see a distinct trend as failure develops: the majority of load-bearing columnar $n$-force chains and their laterally supporting $n$-cycles collapse at failure, consistent with the system becoming severely under-constrained and unstable as $Z_m$ drops below the isostatic condition. As a further confirmation, we also computed the global mean value of the minimum eigenvalue of the particle stress tensor (i.e. the most compressive principal

stress for a particle): in [69], we referred to this as the magnitude of the particle load vector (PLV). The global mean value of the magnitude of the particle load vector may be viewed as an indicator of the load-bearing capacity of the material, in keeping with past knowledge that force chains align in the direction of the most compressive, global principal stress (Figure 10b). We recover the same trends shown previously: destruction of load-bearing force chains is reflected at the global scale by the concurrent loss of load-carrying capacity that is most pronounced after time of 0.04 (0.03) for ESb-S (ESb-K). In sample ESb-S, we observe a small time interval, $0.0538 < t < 0.0606$, in which the material seems to recover and undergo jamming, evident in an increase in the mean particle load vector magnitude in Figure 10b which coincides with the brief increase in force chains shown earlier in Figure 7.

### 3.3. *Cooperative evolution of building blocks*

So far, we have shown that there is consistency in the behaviour of the mesoscopic structural building blocks with those observed globally. The loss of global stability can be traced back to the collective, near-total collapse of the force chains and their supporting contact cycles inside the specimen. Further, we have established that the overall load is carried by only a small fraction of the particles in the system (no more than 22%) and that these particles in force chains are weakly supported from the very start of loading (ESb), with the particles in 3-cycle supports steadily decreasing from the initial value of 25% of the particles in the system. Those particles belonging to both force chain and 3-cycle constitute no more than a mere 12% of the total number of particles. These evolutionary trends at the mesoscopic scale concur entirely with the systems being nearly isostatic at ESb, steadily losing what little redundant constraints it has until the system becomes under-determined and fails catastrophically. That the force chains in the system are just below those in 3-cycles at the start of the loading history ESb leads to the proposition that *the level of truss-like* 3*-cycle supports available in the system may predetermine the growth and manner of evolution of columnar force in the system*.

To test this conjecture, we computed the percentage of 3-cycles supporting force chains (Figure 11). We also pay attention to a small subset of the 3-cycles known as 3-force cycles: 3-cycles where each contact bears the global average force. These have been found to suddenly grow in numbers in systems at the onset of shear banding [27]. We find that typically 80% of 3-cycles are supporting force chains in both samples in regime A. Moreover, this value is almost constant in regime A and in the first phase of regime B, despite a decreasing population of 3-cycles (Figure 8). In sample ESb-S, we observe a small interval of recovery during regime B, between $0.0538 < t < 0.0606$, consistent with the increasing load borne by the particles (Figure 10b). This suggests that the sudden increase in 3-cycle support and the fully dedicated mobilisation of support from the strongest members (i.e. 3-force cycles) to force chains may well be responsible for this residual strength after the time of 0.0538.

A succinct summary of the cooperative behaviour between force chains and 3-cycles is presented in Figure 12. Here, particles are partitioned into two sets: those in force chains, and those not in force chains. We show here the strain evolution of

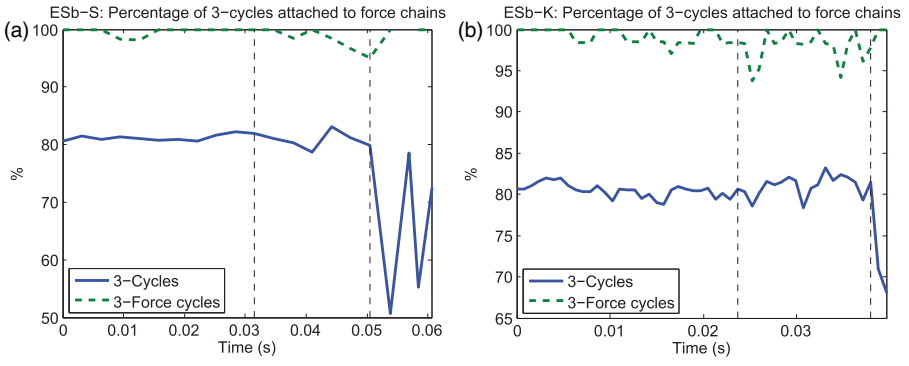


Figure 11. (Colour online) Percentages of 3-cycles and 3-force cycles laterally supporting force chains throughout loading for (a) ESb-S, and (b) ESb-K. No 3-force cycles are present in ESb-S at $t = 0.0569$.

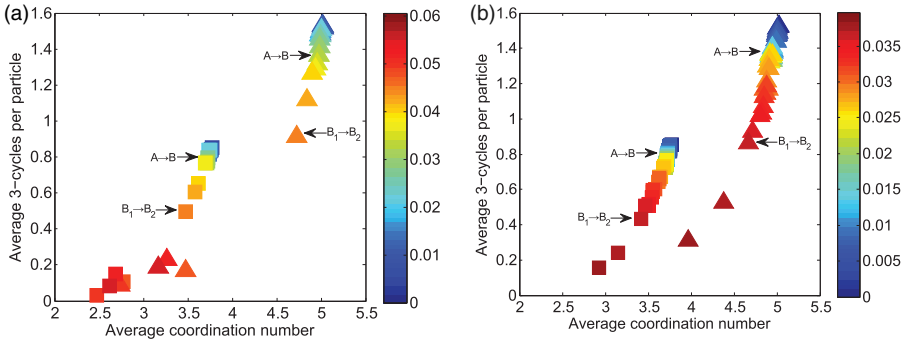


Figure 12. (Colour online) Strain evolution of the number of contacts and 3-cycles per particle in two subsets for (a) ESb-S, and (b) ESb-K. Particles in force chains (△) versus particles not in force chains (□). The legend indicates simulation time.

the number of contacts and 3-cycle membership per particle. Evidence from other DEM simulations, and from photo-elastic disc experiments, in two and three dimensions, and which all experienced localised failure, suggest that force chains reside in local topologies with a higher density of particle contacts in 3-cycles (i.e. higher degree and greater membership of truss-like 3-cycles) [22,27,28,43]. (Note that the degree of a node in complex networks is the number of links for that node; it is therefore the same as the number of contacts or coordination number for a particle if the complex network represents the contact network of the granular material.) Just like those seen for localised failure, force chains in ESb-S and ESb-K also reside in local topologies with a relatively higher density of connections (contacts) in 3-cycle formations, that is, on average, force chains have a higher degree and higher number of 3-cycles in its local contact topology. Particles in force chains typically have degree just below 5, compared to particles not in force chains having degree of just below 4. Similarly, these particles are supported with a greater number of 3-cycles, typically 1.5 per particle, compared to below 1 for non-force-chain particles. These values

drop as the system undergoes failure, but the distinction prevails throughout loading history. Thus the fundamental relationship between 3-cycles and force chains that we observed before in localised failure is also observed in ESb-S and ESb-K. These results show a fundamental *functional* relationship between these building blocks that seems to be generic or universal: 3-*cycles stabilise load-bearing columnar force chains, irrespective of failure mode*.

### 3.4. *Underpinning failure mechanisms*

This section presents two related studies. In the first, we will demonstrate that the samples under consideration fail by force chain buckling. In the second, we will characterise the spatial distribution of not only these underlying failure events but also of the supporting 3-cycles to test the veracity of evidence on buckling. In the latter, a multiscale analysis will be performed at each strain state of the loading history, the objective of which is to establish the extent to which the spatial arrangement of buckled force chains in the sample domain deviates from a perfectly random spatial distribution.

#### 3.4.1. *Macroscopic failure by buckling force chains*

We analysed the evolution of individual force chains and present in Figure 13 the population of force chains which fail by buckling. The algorithm used to generate these results has been described elsewhere [19,27,43] and has been tested against a variety of granular materials in 2D simulations and experiments [19,20,22,23,27,28,41,42] and 3D simulations [43], ranging in particle sizes and shapes, and under different loading conditions, including confined comminution [56]. We find that the collective buckling of force chains causes global failure just as it does in localised failure. The onset of buckling can be seen to coincide with the onset of global instability in regime B. The two values which govern the capture rate in the buckling detection algorithm are varied to demonstrate that the trends are robust: the strain interval or time-step $\Delta t = t_i - t_{i-1}$ and the minimum threshold buckling angle $\theta_b$. As expected, lower values of $\theta_b$ and/or higher $\Delta t$ lead to higher counts on the buckling force chains. Overall, these results show that force chains become overloaded and begin to buckle in regime B. These trends are to be expected given the findings from the preceding sections which showed that the force chains constitute only a small proportion of the entire population of particles (less than 24%), and yet carry more than the global average particle load [69]. Moreover, these columnar structures are weakly supported laterally. Recall that the confining 3-cycles, which initially constitute a mere 25% of the total number of particles in the sample, progressively degrade before dropping to population levels below those for force chains in regime B, consequently predisposing the force chains to collapse by buckling (Figure 9).

#### 3.4.2. *Multiscale spatial distribution analysis*

Although the global failure of the two samples has been shown to be due to the failure of force chains by buckling, we have not yet characterised the spatial

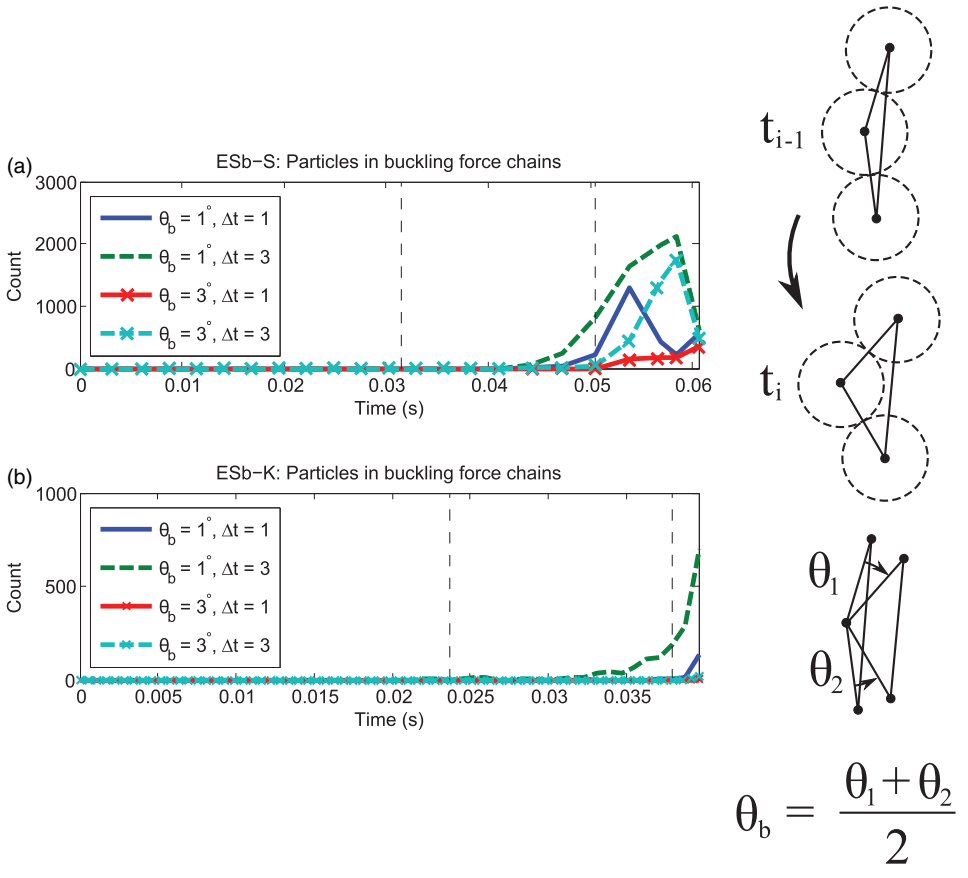


Figure 13. (Colour online) Force chains fail by buckling in both (a) ESb-S and (b) ESb-K. Note that the trends shown here are consistent irrespective of the threshold buckling angle $\theta_b$ (i.e. the minimum buckling angle for the buckling chain to be included in the count) and the strain interval or time-step $\Delta t = t_i - t_{i-1}$ over which buckling occurs (illustration right).

distribution of these buckling events. In samples undergoing localised failure, buckling force chains have been observed to be clustered or concentrated in distinct sub-regions, i.e. shear bands. We now determine whether or not this is the case in these two samples. Specifically, our task here is to quantitatively characterise the spatial distribution of buckling force chains as being localised or diffused. In past studies of spatial patterns, e.g. [74–76], the absence of localisation or clustering is often associated with a random spatial distribution. Accordingly, if the failure events of force chain buckling show evidence to be randomly dispersed with respect to the macroscopic length-scale (i.e. the sample size), then we classify the mode of failure of that sample to be diffused. An additional consideration, designed to test the veracity of the finding on force chain buckling, will be paid to the spatial distribution of the supporting 3-cycles. Overall, our strategy for the characterisation of the spatial patterns formed by buckling force chains and 3-cycles involves two components: (a) the use of a specific statistical function that measures the deviation from spatial

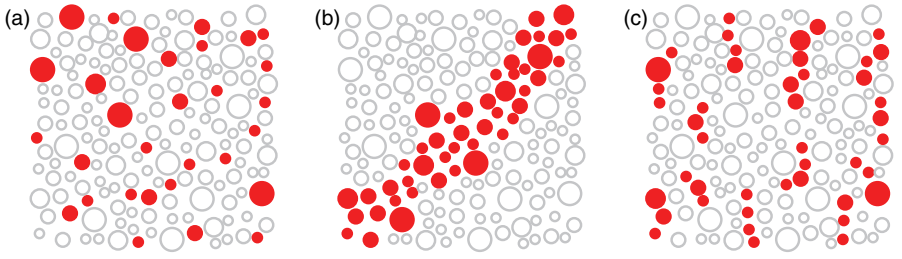


Figure 14. Example illustrations of localisation or clustering of points (shaded circles) at differing length-scales. (a) No clustering or localisation: complete spatial randomness. (b) Localisation. (c) Localisation at small length-scales, complete spatial randomness at larger length-scales.

homogeneity of a given spatial distribution *at multiple length-scales* [77], and (b) a set of random surrogates which allows us to quantify the statistical significance of any deviation from spatial homogeneity of samples ESb-S and ESb-K using the measure in (a). The so-called surrogates are generated by taking the original structures (e.g. buckled force chains) and repositioning them in sample space to achieve a random order of arrangement in the sample domain. In what follows, we will discuss these two components separately in the first two sections (3.4.2.1 and 3.4.2.4), before presenting the results in the last two sections (3.4.2.3 and 3.4.2.4). The results established for ESb-S are qualitatively the same as those found for ESb-K and, as such, we confine the discussion in Sections 3.4.2.3 and 3.4.2.4 to ESb-S only (ESb-K data not shown).

3.4.2.1. *Ripley's K- and L-functions*. Particles within a granular material may be represented by a spatial distribution of points, identified by their particle centres. These points form a set known as a point pattern [74–76,78]. We may similarly represent mesoscopic processes (e.g. force chain buckling) as well as structural motifs (e.g. 3-cycles, 4-cycles, etc.) observed within a deforming granular sample as point patterns. The extent to which a given point pattern deviates from a statistically homogeneous distribution (i.e. isotropy) in space or complete spatial randomness depends on the length-scale in question. Thus, a characterisation of the spatial distribution of force chain buckling necessitates a multiscale spatial analysis [76]. To elucidate the nature of this problem, consider the illustration of contrasting spatial distributions of points (dark circles) in Figure 14. In Figure 14a, points appear randomly distributed, whereas in Figure 14b they appear to be localised. The spatial distribution of points in Figure 14c is mixed. At small length-scales, we observe clustering or localisation, i.e. the points appear clustered into chains. But, if we zoom out and view the pattern at large enough length-scales, then each chain can be envisaged to resolve to a point and the emerging point pattern may appear randomly dispersed in space.

Ripley's *K*- and *L*-functions [74,76,78] are widely used statistical measures to characterise the departure from perfect or complete spatial randomness of point patterns as a function of length-scale. Point patterns fall into three main classes: complete spatial randomness (homogeneous Poisson process), clustering (or

localisation), and regularity. A point pattern is said to exhibit complete or perfect spatial randomness if the points, or events being represented as points, occur in a given spatial domain in a completely random fashion: this asserts that events occur independently of each other. To first order, this distribution may be modelled by a Poisson distribution with one parameter, i.e. the density of points or events, within the prescribed domain. There are two forms of departures from complete spatial randomness. The first is regularity which leads to a lower sub-Poissonian intensity (e.g. points arranged in a grid or lattice). The second is clustering or localisation which leads to a greater super-Poissonian intensity of points than expected for complete spatial randomness.

Ripley's $K$- and $L$-functions summarise the distribution of all inter-point distances for a given point pattern. A point pattern that is fairly regular (e.g. Figure 14a) will have a more uniform inter-point distance distribution than a point pattern that is localised (e.g. Figure 14b) which forms an inter-point distance distribution that is biased towards small length-scales. Specifically, Ripley's $K$- and $L$-functions in three-dimensions are estimated by [79]:

$$K(x) = \frac{V}{n^2} \sum_{i=1}^{n} \sum_{j \neq i}^{n} e_{ij} I[D(i,j) \leq x], \quad L(x) = \sqrt[3]{\frac{3K(x)}{4\pi}}, \tag{6}$$

where $x$ is the observation length-scale, where $V$ is the volume of the sample domain, $n$ is the number of points in the point pattern under consideration, $e_{ij}$ is the edge correction term between points $i$ and $j$, $I[\cdot]$ is the indicator function assuming a value of 1 if $D(i,j) \leq x$ and a value of 0 otherwise, and $D(i,j)$ represents the Euclidean distance from point $i$ to point $j$. Points formed by particles near the sample boundaries are subject to edge effects: they have fewer neighbouring points and correspondingly contribute less to the above summation. We use the three-dimensional counterpart to Ripley's isotropic correction for $e_{ij}$, which is the reciprocal of the proportion of the surface area of a sphere centred at point $i$ with radius $D(i,j)$ which lies within the sample domain (for details, see [79]). Intuitively, the above $K$-function can be considered as a normalised count of points whose inter-point distances fall within some prescribed length-scale $x$. For a homogeneous Poisson point process (i.e. points with complete spatial randomness, as in Figure 14a), Ripley's $K$-function in three-dimensions takes the closed form $K(x) = 4\pi x^3/3$ [79]. A point pattern that is clustered (or localised) as in Figure 14c will have a $K$-function above the closed form – similarly, a regular or grid-like point pattern will be below the closed form. However, due to the large number of points in the point patterns in this study, and the relatively small dimensions of the samples under consideration, deviations in the $K$-function are small. Thus visual comparisons become difficult and uninformative. As such, many studies commonly present results using Ripley's $L$-function, which is simply a rescaled $K$-function, as defined above. The qualitative trends are the same as the $K$-function, but for a homogeneous Poissonian distribution, $L(x) = x$. For clarity, we will present both Ripley's $L$-function and its 'residual' $L(x) - x$.

3.4.2.2. *Randomised surrogates*. Although the above multiscale spatial statistical functions provide a measure of deviation from spatial randomness of a point pattern,

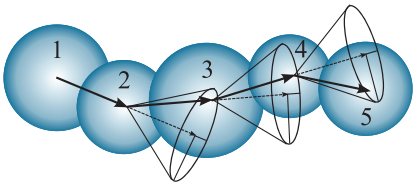


Figure 15. Generation of a single random 5-force chain within a surrogate. A particle (1) with radius chosen from the original particle radius distribution is placed randomly in the sample domain. A random direction is chosen for the next particle. A second particle (2) with similarly random radius is placed in contact with the first. The previous directional vector is duplicated and perturbed to lie within a cone with some apex angle, specifying the direction of the next particle. A particle is placed in contact (3) with the previously placed particle (2). Quasi-linearity of the most recent three particles is checked (1–2–3). Particles continue to be placed in this manner until all five particles are placed. Finally, overall checks are performed for overlaps and position within the domain.

*per se* we are unable to claim if the deviation is of statistical significance. That is, we need a criterion that permits us to discount or reject, to a given significance level, the possibility that the observed pattern is random. To do so, we create randomised surrogates. In essence, each surrogate is generated by taking the original mesoscopic structures (i.e. buckled force chains and 3-cycles) and repositioning them randomly in the sample domain. Many realisations are performed to generate many surrogates. Next, the above Ripley's spatial statistical analysis is then undertaken at various spatial length-scales for both the original sample point pattern and the surrogates: this allows us to compare Ripley's statistic from the original sample against those from the surrogates to within a defined confidence interval. If Ripley's statistic for the original sample lies inside a prescribed confidence interval of the distribution for the surrogates, then the spatial pattern of occurrence of mesoscopic structures in the original sample is indistinguishable with a random spatial distribution.

The deviation from spatial homogeneity of buckling force chains in the original samples is tested for statistical significance by comparing against 1000 surrogates. Each surrogate is realised by randomly placing an equal number and length of buckling force chains over a domain identical to the sample domain. To illustrate this procedure, refer to Figure 15. Consider an $m$-force chain ($m \geq 3$) in the original sample; in Figure 15 the case of $m = 5$ is depicted. To create a chain of $m$ particles in the surrogate system, we begin by selecting a point in the surrogate domain at random. A particle is placed so that its centre is situated at this point. A second particle, in contact with the first, is added in a random direction. The 3rd, 4th, ..., $(m-1)$-th, and $m$-th particles are sequentially added to complete the chain, all while maintaining quasi-linearity, in accordance with the definition of a force chain. This means that the alignment of two adjoining branch vectors (two lines joining the centres of three consecutive particles in the chain) is constrained to be within a tolerance angle of 45°. The direction of each contact or branch vector is chosen randomly within a cone of apex angle of 45°. This parameter permits variability in the misalignment of branch vectors along the chain. The radius of each particle added to the chain is chosen randomly from the particle radius distribution of the original sample without replacement, i.e. a specific particle's radius cannot be

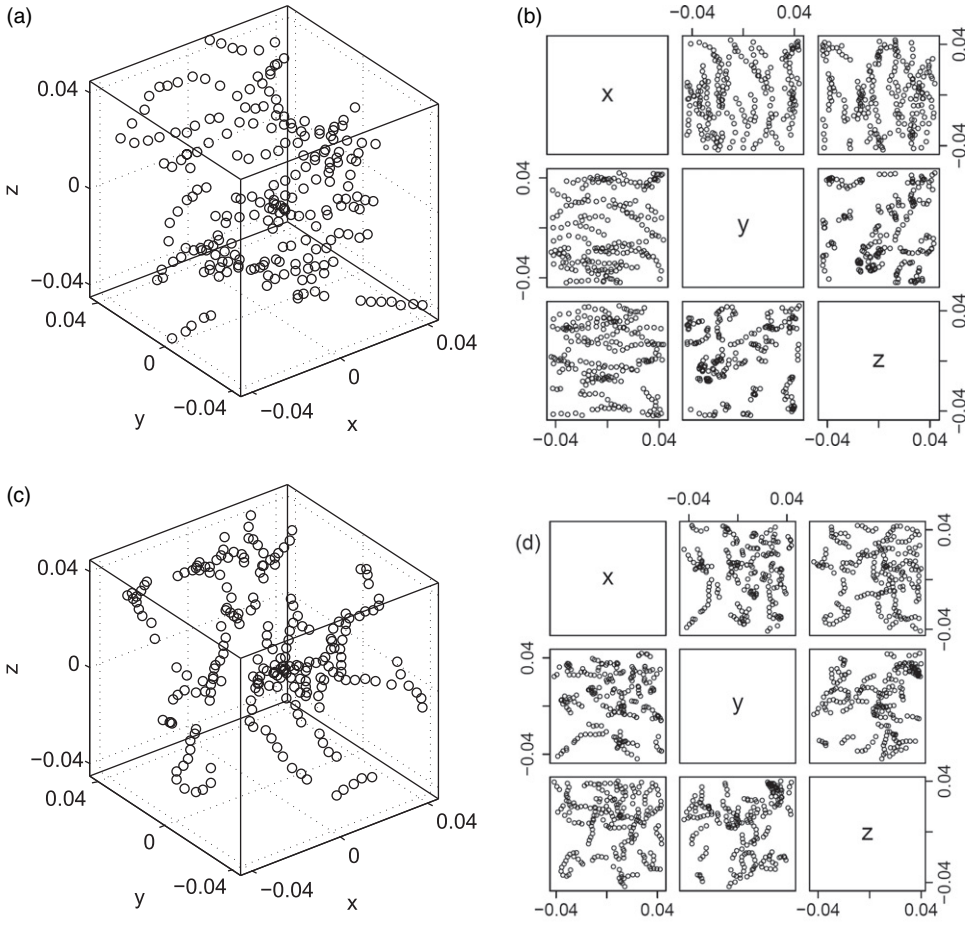


Figure 16. Point patterns formed by particles in buckling force chains at the simulation time interval, $0.0473 \leq t \leq 0.0504$. (a, c) Scatter plots of the points. (b, d) Components of the points. (a, b) ESb-S using capture parameters of $\theta_b = 1^\circ$ and $\Delta t = 1$, consisting of 223 particles in 22 buckling force chains. (c, d) A surrogate of ESb-S at the same simulation time.

selected twice. Overlapping of particle chains is avoided by checking all particles in all placed chains; if any overlap occurs, the most recently placed chain is removed and placement is attempted again. Similarly, a force chain that grows outside the domain is removed and the placement reattempted. No other constraints on proximity to other buckling force chains are enforced. This process is repeated until all buckled force chains in the original sample have been placed in the surrogate system. Figure 16(a, b) shows the distribution of detected buckling force chains within ESb-S at the stage prior to their peak population, and a surrogate (Figure 16c,d) realised using the above described method. The same analysis was performed for all stages (data not shown).

The spatial distributions of 3-cycles is also analysed, with 1000 surrogates. Instead of considering the point pattern formed by constituent particles in 3-cycles, we instead replace each 3-cycle with a point located at the cycles' centre of mass. Each surrogate is then realised by repositioning these points throughout the sample space to achieve a random spatial arrangement. This randomisation by repositioning of the points in space is undertaken subject to a spatial constraint which precludes overlapping among particles. Much in the same way that particles cannot overlap and so must be separated by at least one particle diameter, we similarly enforce that the randomly dispersed points (which keep in mind are actually representing 3-cycles) must be at least $D_m/3$ away from each other, where $D_m$ denotes the mean particle diameter. This minimum value is motivated by considering four spherical particles with equal diameter arranged in a tetrahedron, the most compact arrangement of a group of particles: such an arrangement forms four 3-cycles, the centres of mass of each 3-cycle are subsequently $D_m/3$ units away from each other. When generating the surrogates, points found violating the condition of no-overlap are repositioned in the sample domain. This is repeated until the condition of no-overlap is satisfied. Figure 17 shows the point patterns formed by reducing 3-cycles to points within ESb-S corresponding to the transition $A \rightarrow B$ in the loading history (Figure 17a,b), and a surrogate realised using the above method (Figure 17c,d).

3.4.2.3. *Spatial distribution of buckling force chains*. Keep in mind that we only discuss here the results established for ESb-S, as those for ESb-K are qualitatively similar and belong to the same class of point pattern as ESb-S. The spatial distribution of particles in buckling force chains is analysed and its departure from complete spatial randomness is presented in Figure 18. This figure shows the computed Ripley $L$-function and its residual $L(x) - x$ applied to point patterns formed by particles found to be in buckling force chains, as discussed earlier in Section 3.4.1. In particular, the results in Figure 18 are for that interval of the loading when the number of particles in buckling force chains in sample ESb-S reaches a maximum: $0.0504 \leq t \leq 0.0538$ which is in the latter stages of regime B ($B_2$) for $\theta_b = 1$ and $\Delta t = 1$ in Figure 13. The sensitivity of the above thresholds has been studied extensively [19,20,27,41,69,80] and the choices here are perfectly reasonable. The distribution of particles in buckling force chains at the previous stage (chosen for clarity), $0.0473 \leq t \leq 0.0504$, is shown in Figure 16a, b. The length-scales considered are up to half the shortest side length of the cuboidal sample, which is approximately 10 particle diameters: values higher than this are subject to and incur significant boundary effects. A 95% confidence interval is estimated by computing the $L$-function for the 1000 randomised surrogates.

Complete spatial randomness in a point pattern is presented by the homogeneous Poisson process, i.e. the line $L = x$ in Figure 18a or the horizontal line $L(x) - x = 0$ in Figure 18b. Hence, a failure pattern that is said to exhibit complete spatial randomness is one where the underlying failure events occur independently of each other and are randomly distributed in space. This asserts that there is equal probability of finding such an event anywhere in the sample space and events do not interact with each other (i.e. the occurrence of one failure event does not prohibit nor promote the occurrence of another). At length-scales below the smallest particle

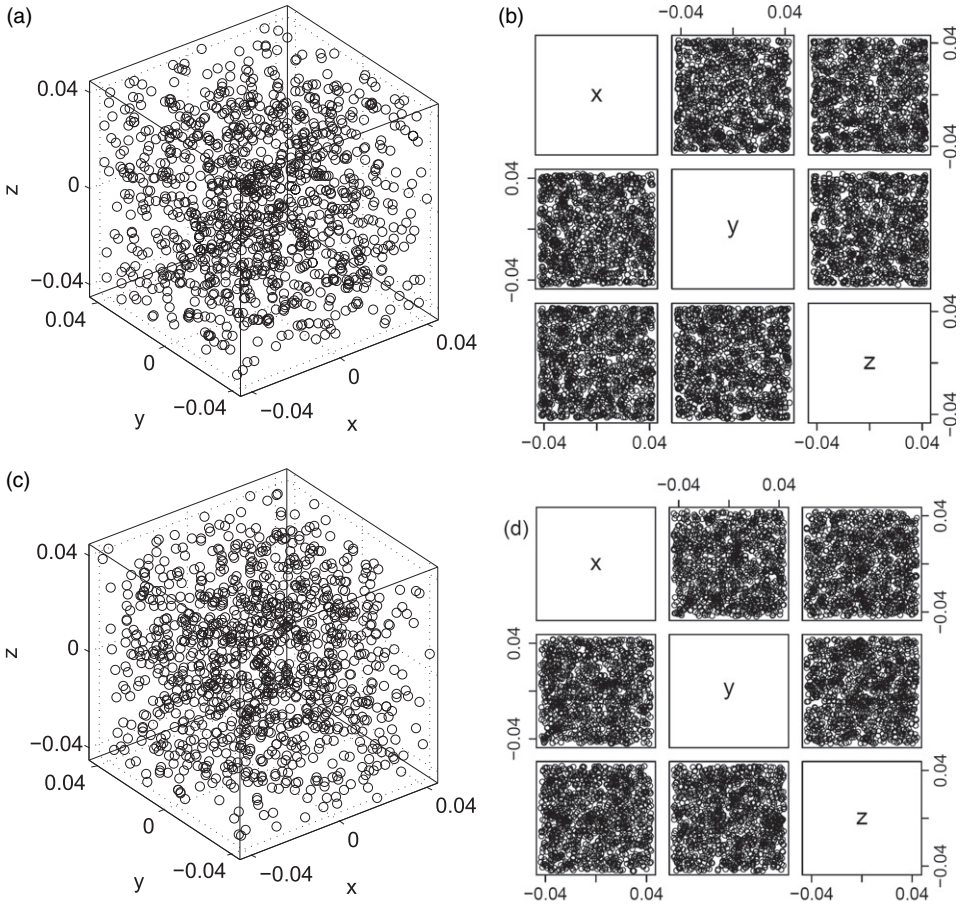


Figure 17. Point patterns formed by 3-cycles. (a, c) Scatter plot of the points. (b, d) Components of the points. (a, b) ESb-S at $t = 0.0315$ consisting of 1149 points. (c, d) A surrogate of ESb-S at the same strain stage.

diameter, the $L$-function and its residual are both zero. This is expected, as particles cannot be closer to each other than the minimum particle diameter. For length-scales between $D_m$ and $2D_m$, where $D_m$ is the mean particle diameter, the $L$-function and its residual for ESb-S and its surrogates both lie above the Poisson expectation, thereby suggesting some clustering is present. This is to be expected because, by definition, force chains are groups of at least three particles clustered in a quasi-linear formation; recall also that 3-force chains form the most dominant class in the force chain network of both samples studied here (Figure 7).

Note that the $L$-function for ESb-S over length-scales just above $D_m$ is below the confidence envelope established from the realised surrogates, suggesting greater levels of clustering are realised in these surrogate systems than the buckled force chains in ESb-S. In creating the surrogates, no constraint was placed on the proximity between buckling force chains apart from the condition of no-overlap.

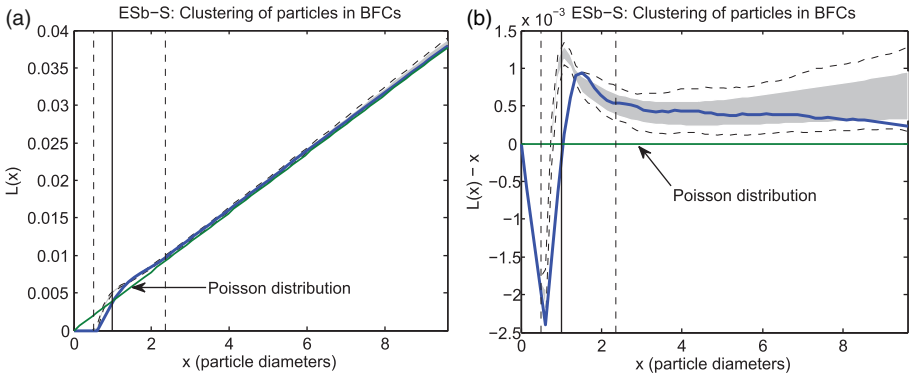


Figure 18. (Colour online) (a) Ripley $L$-function, and (b) residuals computed for particles in buckling force chains for ESb-S at $0.0473 \leq t \leq 0.0504$, compared to complete spatial randomness (green). Confidence interval of 1000 surrogates (grey) and maximal/minimal values attained by surrogates (dashed). Vertical lines correspond to smallest (dashed), mean (solid) and largest (dashed) particle diameters respectively.

Therefore it is possible for force chains in the surrogates to lie side by side or for member particles from distinct force chains to be in contact. In other words, buckling force chains in ESb-S are more regularly spaced than its surrogates, i.e. there is more space between buckling force chains. This may be due to the attendant local dilatation that is inherent in force chain buckling [19,20].

Finally, as we zoom out to larger macroscopic length-scales, the $L$-function for ESb-S and its surrogates becomes indistinguishable. The residual shows that the distribution of force chain buckling in ESb-S tracks those from the randomised surrogates, lying within the 95% confidence interval at length-scales above two particle diameters. The gradual increase in clustering of surrogates at the largest length-scales is due to boundary effects, and the difficulty in randomly placing force chains near the sample domain boundaries. Although buckling force chains in ESb-S do not exhibit a perfectly random spatial distribution, the deviation is of no statistical significance and is indistinguishable with the spatial distribution of the randomised surrogates.

For the purposes of comparison, we include in Figure 19 the corresponding Ripley $L$-function and its residual for the system in [43] which undergoes localised failure: here we see a striking difference between the sample and its realised surrogates at *all* length-scales greater than the mean particle diameter, indicating significant clustering when compared to surrogates embodying randomly distributed buckling force chains. Thus, using the strategy adopted here, the conclusion that the failure for that system was indeed due to localisation of buckling force chains is hereby confirmed.

3.4.2.4. *Spatial distribution of 3-cycles.* To gain a deeper understanding of why the buckling events are diffused or randomly dispersed throughout the domain of sample ESb-S, a similar study was undertaken of the spatial distributions of its 3-cycles,

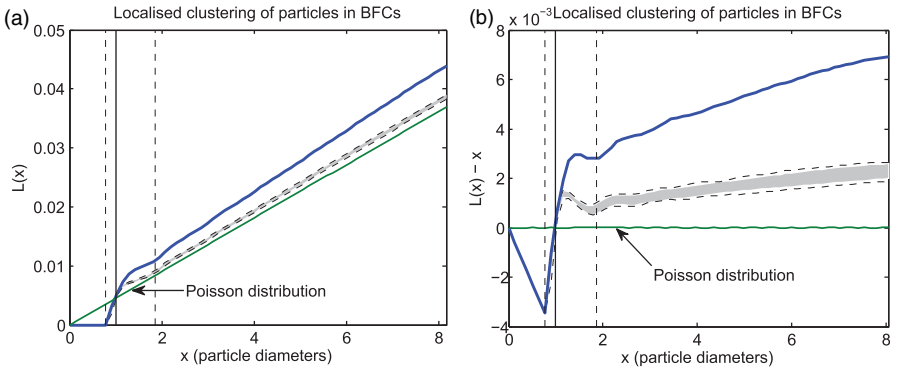


Figure 19. (Colour online) (a) Ripley $L$-function, and (b) residuals computed for particles in buckling force chains for a system that undergoes localised failure in [43].

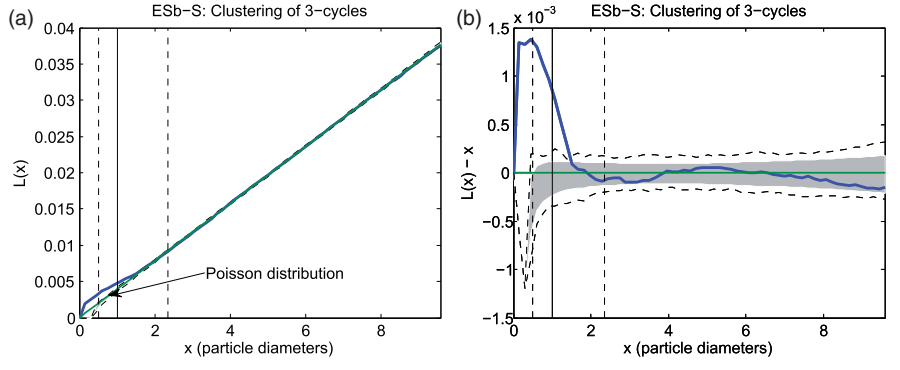


Figure 20. (Colour online) (a) Ripley $L$-function, and (b) residuals computed for centres of mass of 3-cycles for ESb-S at $t = 0.0315$, compared to complete spatial randomness (green). Confidence interval of 1000 surrogates (grey) and maximal/minimal values attained by surrogates (dashed). Vertical lines correspond to smallest (dashed), mean (solid) and largest (dashed) particle diameters respectively.

as shown in Figure 20. The results presented correspond to the transition $A \rightarrow B$ of the loading history ($t = 0.0315$), the point at which 3-cycles begin to degrade and force chains lose their stabilising agents (recall Figures 8 and 12). The distribution of 3-cycles at this time is shown in Figure 17a, b. Statistical significance of deviations is compared against confidence intervals corresponding to 95% of all surrogates. With respect to small length-scales below the maximum particle diameter, the point patterns of the centres of masses of the 3-cycles exhibit clustering: the $L$-function (Figure 20a) and its residuals (Figure 20b) take values higher than both the realised surrogates and the complete spatially random (Poisson) distribution. This suggests that 3-cycles within ESb-S are in closer proximity to each other in certain parts of the sample than those found in the randomised surrogates and in a perfectly random system. This is consistent with the earlier result uncovered in Figure 12 where 3-cycles are found in greater densities around force chains within the sample, which

would indeed bias this measure to smaller length-scales not accounted for in our surrogates. However, if we zoom out and examine the sample at a slightly larger length-scale, i.e. at and above the maximum particle diameter, we find no difference of statistical significance between the $L$-function, the realised surrogates, and complete spatial randomness. This trend prevails at the larger spatial scales, suggesting that 3-cycles are randomly dispersed throughout ESb-S with no statistically significant evidence of clustering or regularity. Additionally, these trends are common throughout the loading history, right back to the initial stage ESb. Finally, the spatial distributions of 3-cycles in ESb-K throughout loading are entirely consistent with those reported here for ESb-S.

### 3.5. *Birth-and-death of processes of 3-cycles and 3-force chains*

At the start of this paper, we underlined the principles advanced by Hill [25] and Rice [26] – that understanding the essential mesoscopic structural rearrangements inside the deforming material is key to developing robust constitutive models of observed inelastic macroscopic behaviour. The preceding analysis in Section 3.4 focused on the distribution of structural building blocks with respect to space. To gain a deeper insight into these structural rearrangements, we now complement this study with an exploration into the evolution of structural building blocks with respect to time. Of all such structures, the 3-cycles and 3-force chains arguably exert the greatest influence on the material's load-carrying capacity. 3-Cycles are the most important of all the minimal contact cycles in supporting force chains, and are thus key topological structures underlying the shear strength of granular materials. On the other hand, the 3-force chains form the most dominant class in the force chain network of both systems. These factors prompt a detailed analysis of birth-and-death processes and lifetimes of these fundamental structures, initially investigated in [43] for a 3D sample which undergoes localised failure.

Figure 21 presents the time distribution of 3-cycle births and deaths. A 3-cycle is born when three particles come together to form a mutual contact. We track the evolution of each such structure in the simulation until its collapse or death. The initial peak in the distribution of births corresponds to the initial population of 3-cycles in the contact network at ESb. In regime A, 3-cycle birth-and-death rates are low and almost balanced, with a modest net loss on the overall 3-cycle population, hence the slow decrease seen earlier in Figure 8. In the transition into regime B, 3-cycle birth-and-death rates suddenly increase linearly to a peak. Here death rates can be seen to exceed birth rates by nearly double, before a sudden drop in births and deaths in phase 2 of regime B, during the samples' collapse.

The peak in 3-cycle deaths, simultaneous with the smaller peak in the 3-cycle births, gives rise to the significant changes evident in the macroscopic behaviour of each of the samples: the vanishing of stress (Figures 3 and 4), the lowest mean mechanical coordination value (Figure 10a) and lowest mean particle load vector magnitude (Figure 10b). Importantly, the marked increase in 3-cycle birth-and-death rates from regimes A to B reflect significant internal rearrangements among these important structures – that is not readily apparent in earlier measures. The mechanical coordination number (Figure 10a) gives no indication that there is a

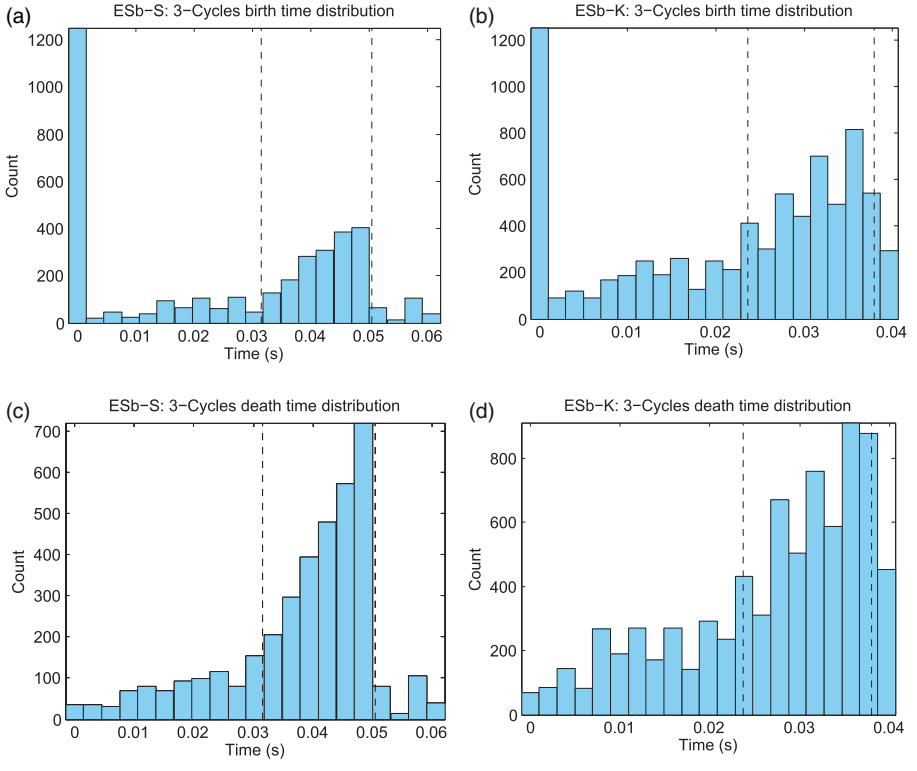


Figure 21. Frequency distribution of (a, b) 3-cycle births, and (c, d) 3-cycle deaths, for (a, c) ESb-S, and (b, d) ESb-K.

sudden change in activity within the material and Figures 3, 4, 8 and 10 are macroscopic measures that provide only a hint of the mesoscopic activity uncovered here.

The 3-cycle lifetimes are also informative, particularly at the two extremes: the shortest and longest lifespans. The former reflects unsustainable structural reorganisations and is indicative of large deformations and instability, while the latter unearths the existence of relatively stable regions in the sample. Figure 22 presents the distributions for the most transient, short lived 3-cycles, which exist only for a single time-step in the simulation. By combining this information with that in Figure 21, we find that the subset of short-lived 3-cycles is in fact the primary contributor to the birth-and-death processes in Figure 21. For ESb-S, observe that essentially the fewest short-lived 3-cycles emerge in regime A, corroborating earlier evidence of a relatively stable response to the applied load over these stages of the loading history. The gradual increase in the transient 3-cycles during regime A for ESb-K explains the loss of load-carrying capacity that is most evident in Figure 10b. Transitioning into regime B, we see from Figure 22 a sudden increase in the intensity of structural reorganisations in the sample as the populations of short-lived 3-cycles rises to a peak, at the same stage in the simulation that births and deaths reach a maximum (recall Figure 21).

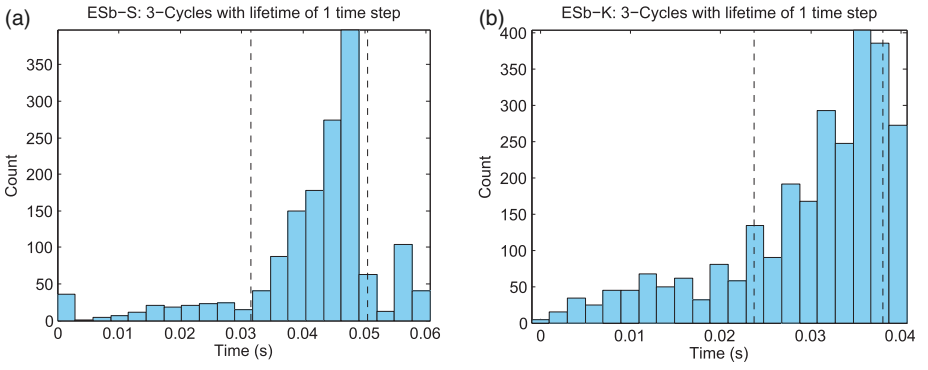


Figure 22. Frequency distribution of short-lived 3-cycles – those which live for only one simulation time step – for (a) ESb-S and (b) ESb-K.

At the other extreme, we examined those 3-cycles in the *initial* contact network at ESb to see if any of these survive the whole loading history. The motivation for this comes from the fact that in localised failure, some cycles in the stable zones of the material (i.e. those outside the shear band) persist throughout the entire loading history: see the inset of Figure 23c. We tracked the evolution of the 3-cycles from the initial population and found *none* of them survive failure in ESb-S and the same can be said essentially of ESb-K: Figure 23a, b. Notice also certain stages for ESb-K, i.e. $0.005 < t < 0.015$ in regime A, during which there is a rise in deaths of 3-cycles from this initial population. We suspect this is due to the nature of the perturbation applied to this sample, i.e. randomly selected particles which are not part of the contact network are each given a small instantaneous velocity in a random direction. The collisions between these particles and the already near-isostatic contact network may be sufficient to trigger a cascade of 3-cycle rearrangements at this time. Overall, the age distributions of 3-cycles is heavily biased towards short-lived 3-cycles: see the peak at one time-step in the simulation in Figure 23c, d.

We now turn our attention to the 3-force chains. Figure 24 presents the time distribution of their births, similarly tracking the manner of evolution of 3-cycles (Figure 21). The highest rates of 3-force chain births and deaths occur in regime B, suggesting that the greatest structural rearrangements among these load-bearing columns coincide with the onset of force chain buckling. Just like short-lived 3-cycles, short-lived 3-force chains exist only for a single step of the simulation (Figure 25). These exist in small numbers for both ESb-S and ESb-K in regime A, with their population staying mostly constant. Again upon the transition into regime B, there is a marked and linear increase in their population, rising to a peak essentially at the same time when buckling events peak for each respective system (ESb-S 0.0504 and ESb-K 0.0379), with ESb-S recovering marginally until the end of the simulation. In much the same way that short-lived 3-cycles account for the majority of 3-cycle births and deaths, short-lived 3-force chains account for almost all 3-force chain births and deaths. Note that the maximum populations of short-lived 3-force chains coincide with the peak in buckling events, which is when the

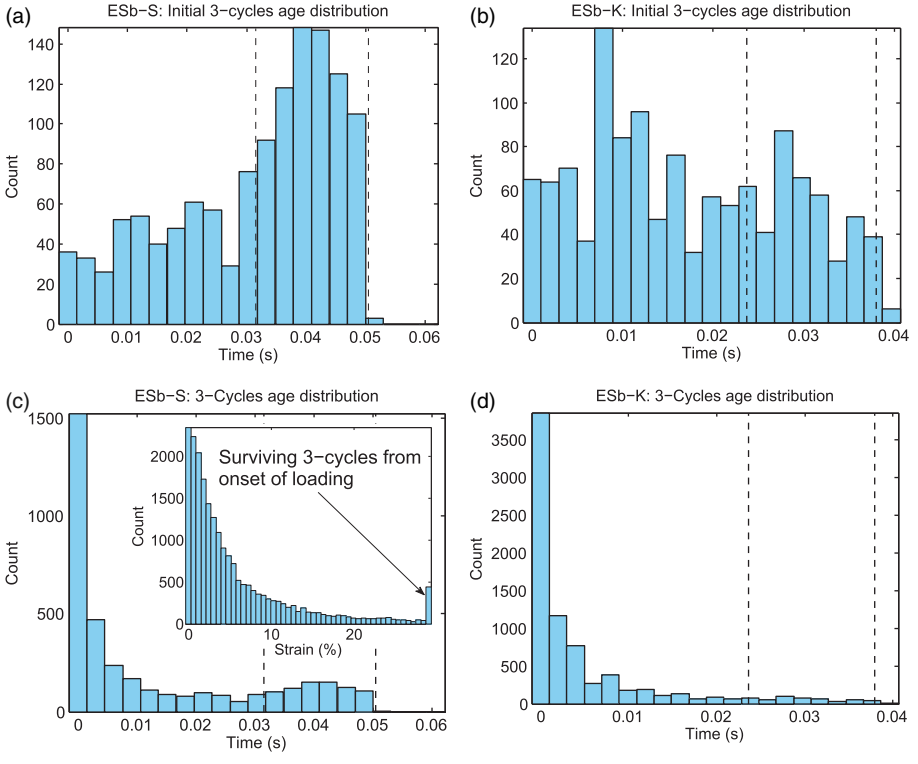


Figure 23. Frequency distribution of (a, b) the ages of only those 3-cycles in the *initial* 3-cycle network born at the initial stage of loading history, and (c, d) of *all* 3-cycles irrespective of time of birth, for (a, c) ESb-S, and (b, d) ESb-K. (c inset) Age distribution of all 3-cycles in the 3D system reported in [43] which undergoes localised failure: recall the results of the spatial point pattern analysis for this system in Figure 19.

material is mostly undergoing internal deformation. This behaviour has also been observed in systems undergoing localised failure.

We present in Figure 26, the age distributions of 3-force chains, beginning with those in the *initial* network ESb, followed by those for all 3-force chains irrespective of time of birth. None of the 3-force chains from the initial state ESb survive throughout loading. In fact, in both samples, none of the initial 3-force chains survive beyond their respective sample collapse times at $t = 0.0504$, and the vast majority of them collapse by the onset of force chain buckling. The large initial peak in the overall age distributions correspond to short-lived 3-force chains also explored earlier for 3-cycles (recall Figure 25). The rapid decay indicates that most 3-force chains live for only a short time, with only a few isolated chains being able to survive longer than half of the loading history, which is consistent with the earlier findings which suggest that force chains in the two systems, even from the beginning of the simulation, are generally weakly supported and near-isostatic – just as the overall samples are also near-isotatic: recall regime A in Figures 10a and 12. The weak support and low redundancy of force chains implies that these axially loaded particle

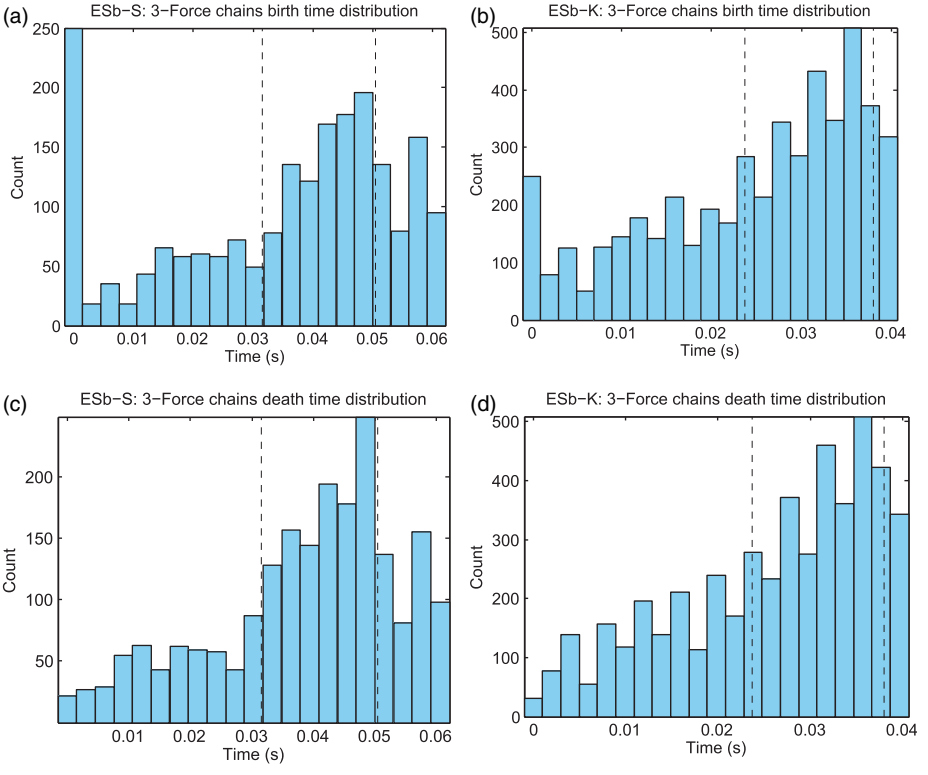


Figure 24. Frequency distribution of (a, b) 3-force chain births, and (c, d) 3-force chain deaths, for (a, c) ESb-S, and (b, d) ESb-K.

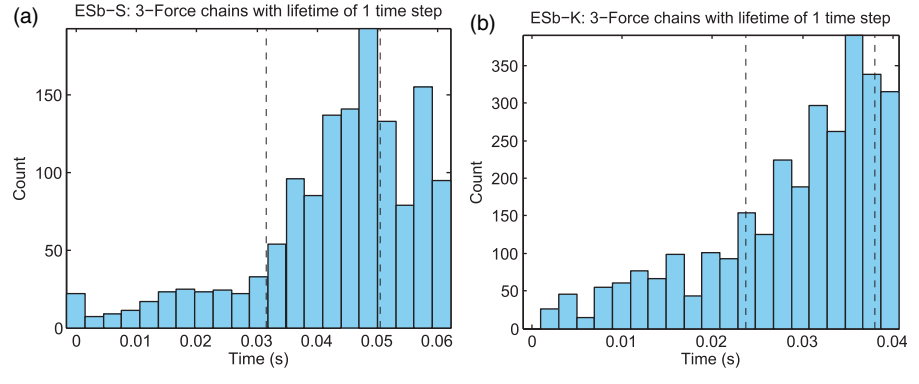


Figure 25. Frequency distribution of short-lived 3-force chains – those which live for only one simulation time step – for (a) ESb-S and (b) ESb-K.

columns are readily overloaded without any capacity for member particles to redistribute the forces in the absence of physical rearrangements.

In statically indeterminate or redundant systems comprising many constituent columnar members, failure by buckling of one load-carrying member does not

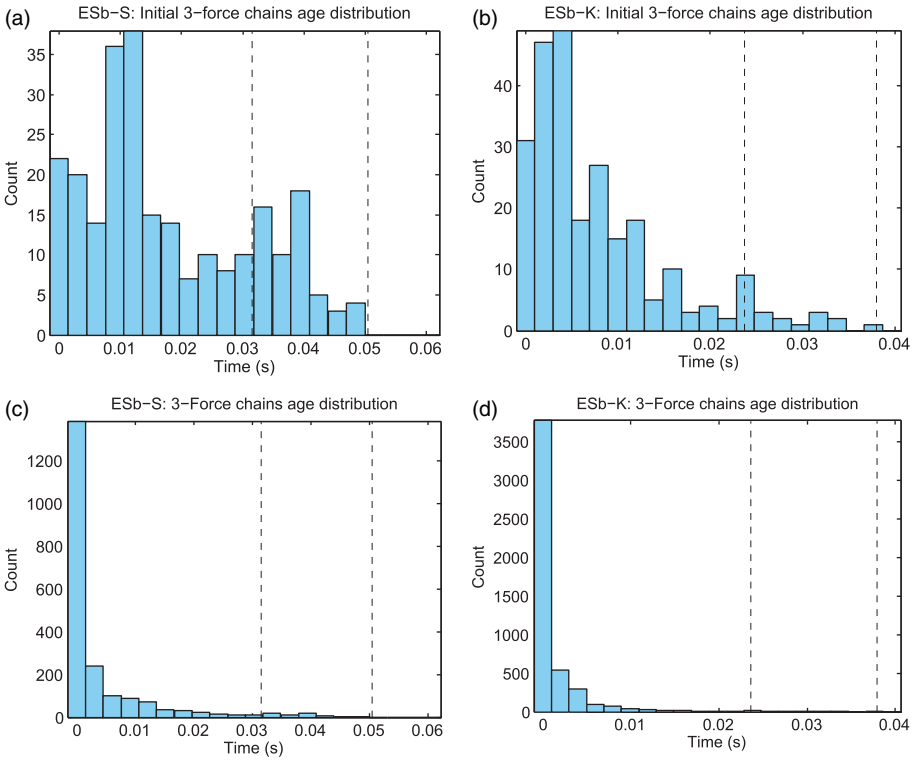


Figure 26. Frequency distribution of (a, b) the ages of only those 3-force chains in the *initial* force chain network born at the initial stage of loading history, and (c, d) of *all* 3-force chains irrespective of time of birth, for (a, c) ESb-S, and (b, d) ESb-K.

usually mean the global collapse of the structure. Redundancy means that forces in the system can redistribute among the members, allowing the load borne by the system to further increase, until another member is overloaded and fails by buckling, and so forth. This process continues until some critical point is reached, when a sufficient number of the constituent members have buckled that the whole structure collapses [71]. The samples ESb-S and ESb-K were perturbed at a near-isostatic state ESb, from which there is little capacity for a redistribution of forces without triggering actual physical rearrangements of the constituent particles and, in turn, the failure of structural building blocks. The birth-and-death processes and lifetimes uncovered here reveal the fine details of these rich structural rearrangements, suddenly intensifying at the onset of force chain buckling, ultimately precipitating the samples' global collapse. In examining the spatial distribution of the 3-cycles supporting the force chains, we found no evidence of clustering throughout the specimen (Section 3.4.2.4). This implies that there are no subregions of the sample where force chains are sufficiently supported to be resistant against buckling. That all of the 3-cycles, and for that matter, all $n$-cycles irrespective of size $n$, collapse indicates that the samples are bereft of support everywhere in the final stages (regime $B_2$) of loading. This may therefore explain the resultant manner of failure by

buckling of the major load-bearing columns which proves to be globally dispersed in these samples (recall Section 3.4.2.3). By contrast, we observe relatively stable zones in localised failure, situated on either side of where the shear band ultimately develops [27]. Such stable zones are populated by a subset of 3-cycles which support and provide resident force chains the redundant constraints necessary to achieve force rearrangements without incurring large structural rearrangements; indeed, these zones are essentially undeforming and move in an almost rigid body manner once the band is fully developed. This subset of 3-cycle topologies, residing completely in the zones outside the shear band region, is especially stable and survives the entire loading history, well into the so-called 'critical state' regime when the shear band is fully developed. Thus shear bands and this set of stable and persistent 3-cycles are mutually exclusive in space but not in time. Samples ESb-S and ESb-K present no such subset of 3-cycles.

## 4. Conclusion

We have established a number of key findings on the microstructural evolution inside deforming granular materials in the lead up to and during the so-called 'diffuse failure' – a mode of failure in the absence of strain-localisation at the macroscopic spatial scale. Granular rheology observed at the macroscopic scale is a manifestation of significant inelastic structural rearrangements among the basic building blocks of self-organisation at the mesoscopic scale, i.e. the quasi-linear and cyclic structures of $m$-force chains and $n$-cycles, respectively. Here, we have characterised the evolution of these structures and found that the essential structural rearrangements can be distilled down to a *cooperative evolution* among the major load-bearing force chains and their supporting 3-cycles, with force transmission pathways exploiting all the benefits that 3-cycle contact topology has to offer. Force chains preferentially reside in those parts of the contact network where 3-cycles exist and can consequently mobilise resistance to the inevitable failure by buckling. This cooperative evolution between force chains and 3-cycles also holds true for systems that undergo localised failure. Truss-like 3-cycles not only laterally support axially loaded, column-like force chains, but also frustrate relative rotations which are key mechanisms for instability at contacts.

We found *prima facie* evidence that the level and spatial distribution of support provided by 3-cycles initially present in the material *predetermines* the development and ultimately the failure of force chains. In the specimens examined here, 3-cycle supports are in short supply and form a minority subset of the minimal contact cycle bases. These supports are indistinguishable from complete spatial randomness throughout the sample domain, right from the start of loading through to and during failure; thus, irrespective of location in the sample and stage of loading, the force chains are very weakly supported, are prone to, and indeed ultimately fail by buckling. The total loss of bulk load-carrying capacity is decidedly due to the precipitous near-total collapse of all the structural building blocks. These trends are in contrast with those observed from specimens undergoing localised failure. In such systems, 3-cycles form the majority of the minimal cycle bases for essentially all of the loading history and there is a relatively large number of 3-cycle supports per force

chain particle – except in the shear band region where force chain buckling ends up being confined; destruction of the structural building blocks is consequently partial only, thereby leaving the material with some residual load-carrying capacity in the so-called critical state regime.

We performed a multiscale point-pattern analysis of the spatial distribution of the failure event of force chain buckling using Ripley $K$- and $L$-functions. At large macroscopic length-scales, we find these to be essentially random exhibiting a pattern that is close to complete spatial randomness, as governed by a homogeneous Poisson process, wherein the underlying failure events occur independently of each other. More specifically, this finding suggests that there is equal probability of finding such an event anywhere in the sample space and buckling events do not interact with each other (i.e. the occurrence of one failure event does not prohibit nor promote the occurrence of another). To test the veracity of evidence on force chain buckling, we performed two additional tests. The first test involved the development of 1000 randomised surrogates of each of the samples, at every strain state during which buckling occurred, in order to establish a confidence interval. Each surrogate is realised by randomly placing an equal number and length of buckling force chains over a domain identical to the sample domain. The Ripley $L$-function showed that the spatial distribution of buckled force chains in the original samples lies well within the 95% confidence interval of their respective randomised surrogates, thus corroborating the earlier result that the buckling events are indistinguishable from spatial randomness. The second test repeated the entire multiscale point-pattern analysis, including the construction of surrogates to establish a 95% confidence interval, but this time focusing on the spatial distribution of supporting 3-cycles – again at those strain states when buckling occurred – and at the initial state. The finding is the same as that established for force chain buckling, i.e. 3-cycles in the specimens are also indistinguishable from complete spatial randomness – from the very beginning of the loading programme. Altogether, the evidence gathered here shows that the failure processes of force chain buckling and the emergence of associated 3-cycles supports occur *in the absence of localisation*.

In past studies, the most stable structures were found to be the 3-cycles and 3-force chains. Here we discover a rich pattern of inelastic structural rearrangements at the mesoscopic scale, evident in the patterns of birth-and-death and the lifetimes of these structures. The greatest number of inelastic structural rearrangements in the material occur at a stage in the loading history when the forces chains become overloaded and fail by buckling. Essentially all 3-cycles, irrespective of when and where they emerge, are completely destroyed during these stages. This is in distinct contrast to specimens which fail via strain localisation, in which a fraction of 3-cycles outside the region of force chain buckling, i.e. outside the shear band, persist throughout the entire loading history, thereby coincident with the fully developed shear band in time but not in space. The spatially random occurrence of force chain buckling, the absence of persistent 3-cycles and, more broadly, the near total collapse of all structural building blocks – hints at a possible signature of diffuse failure. Of course, the universality of the trends reported here for diffuse failure can only be judged by making additional measurements both in simulations and experiments. The latter is decidedly fraught with severe difficulties. Arguably the biggest challenge confronting experiments is the catastrophic nature of the diffuse failure mode.

The internal structure of the material changes rapidly in this dynamic regime; hence direct measurements prove exceptionally difficult once the course of failure has commenced.

In summary, together with force chains, the 3-cycles emerge as a defining class of structural building blocks that is critical to the load-carrying capacity and mode of failure of the material at the macroscopic scale. Their co-evolution with force chains and the underpinning failure of force chain buckling are fundamental mechanisms which seem to be generic to the rheology of dense granular materials, irrespective of the mode of failure. The fine details of their evolution, however, leave behind a unique footprint which offers clues on why a particular mode of failure may be favoured over another. The insights gained on the spatio-temporal evolution of these structural building blocks lay bare the foundation for the development of micromechanical continuum models which can reproduce both localised and diffuse modes of failure. Work on this front is underway.

**Acknowledgements**

AT and SP was supported by the US Army Research Office Grant (DAAD-W911NF1110175), the Australian Research Council Discovery Projects (DP0986876 and DP120104759), the Melbourne Energy Institute Major Research Projects and Initiatives, Development Support Fund, and the Gilbert Riggs PhD Scholarship (SP). We thank David M. Walker, Jacques Desrues and Pierre-Yves Hicher for insightful discussions.

**References**

[1] M. Oda and H. Kazama, Géotechnique 48 (1998) p.465.
[2] K. Ikeda, Y. Yamakawa, J. Desrues and K. Murota, Phys. Rev. Lett. 100 (2008) p.198001.
[3] J. Sulem and I. Vardoulakis, *Bifurcation Analysis in Geomechanics*, Vol. 1, Chapman & Hall, London, 1995.
[4] J. Desrues and I.O. Georgopoulos, Soils Found. 46 (2006) p.585.
[5] C. Granell, S. Gómez and A. Arenas, Chaos 21 (2011) p.016102.
[6] J. Desrues and G. Viggiani, Int. J. Numer. Analyt. Meth. Geomech. 28 (2004) p.279.
[7] P.V. Lade, Int. J. Solids Struct. 39 (2002) p.3337.
[8] P.V. Lade and D. Pradel, J. Eng. Mech. 116 (1990) p.2532.
[9] A. Daouadji, F. Darve, H. Al Gali, P.Y. Hicher, F. Laouafa, S. Lignon, F. Nicot, R. Nova, M. Pinheiro, F. Prunier, L. Sibille and R. Wan, Int. J. Numer. Analyt. Meth. Geomech. 35 (2011) p.1731.
[10] L. Sibille, F.V. Donzé, F. Nicot, B. Chareyre and F. Darve, Acta Geotech. 3 (2008) p.15.
[11] L. Sibille, F. Nicot, F. Donzé and F. Darve, Eur. J. Environ. Civ. Eng. 13 (2009) p.187.
[12] A.L. Rechenmacher, J. Mech. Phys. Solids 54 (2006) p.22.
[13] S.A. Hall, D.M. Wood, E. Ibraim and G. Viggiani, Granular Matter 12 (2010) p.1.
[14] G. Viggiani, *Mechanisms of localized deformation in geomaterials: An experimental insight using full-field measurement techniques*, in *Mechanics of Natural Solids*, D. Kolymbas and G. Viggiani, eds., Springer, Berlin, 2009, p.105.
[15] D.M. Walker, A. Tordesillas, S. Pucilowski, Q. Lin, A. Rechenmacher and S. Abedi, Int. J. Bifurc. Chaos (2012) (in press).
[16] K. Iwashita and M. Oda, Powder Technol. 109 (2000) p.192.

[17] G. Viggiani, N. Lenoir, P. Bésuelle, M. Di Michiel, S. Marello, J. Desrues and M. Kretzschmer, C.R. Mec. 332 (2004) p.819.
[18] J. Desrues, G. Viggiani and P. Bésuelle, *Advances in X-ray Tomography for Geomaterials*, John Wiley, New York, 2006.
[19] A. Tordesillas, Phil. Mag. 87 (2007) p.4987.
[20] A. Tordesillas, J. Zhang and R.P. Behringer, Geomech. Geoeng. 4 (2009) p.3.
[21] A. Rechenmacher, S. Abedi and O. Chupin, Géotechnique 60 (2010) p.343.
[22] A. Tordesillas, Q. Lin, J. Zhang, R.P. Behringer and J. Shi, J. Mech. Phys. Solids 59 (2011) p.265.
[23] J. Zhang, T.S. Majmudar, A. Tordesillas and R.P. Behringer, Granular Matter 12 (2010) p.159.
[24] F. Darve, L. Sibille, A. Daouadji and F. Nicot, C.R. Mec. 335 (2007) p.496.
[25] R. Hill, J. Mech. Phys. Solids 6 (1958) p.239.
[26] J.R. Rice, J. Mech. Phys. Solids 19 (1971) p.433.
[27] A. Tordesillas, D.M. Walker and Q. Lin, Phys. Rev. E 81 (2010) p.011302.
[28] A. Tordesillas, P. O'Sullivan, D.M. Walker and Paramitha, C.R. Mec. 338 (2010) p.556.
[29] F. Darve and X. Roguiez, *Homogeneous bifurcation in soils*, in *Fourth International Conference on Localization and Bifurcation Theory for Soils and Rocks*, A. Toshihisa, F. Oka and A. Yashima, eds. (Gifu, Japan), Balkema, The Netherlands, 1998, p.43, ISBN: 9058090043.
[30] F. Alonso-Marroquín, I. Vardoulakis, H.J. Herrmann, D. Weatherley and P. Mora, Phys. Rev. E 74 (2006) p.031306.
[31] F. Darve, G. Servant, F. Laouafa and H. Khoa, Comput. Meth. Appl. Mech. Eng. 193 (2004) p.3057.
[32] H.D.V. Khoa, I.O. Georgopoulos, F. Darve and F. Laouafa, Comput. Geotechnics 33 (2006) p.1.
[33] J.D. Eckersley, Géotechnique 40 (1990) p.489.
[34] J.A. Sladen, R.D. D'Hollander and J. Krahn, Can. Geotech. J. 22 (1985) p.564.
[35] J. Chu, S. Leroueil and W.K. Leong, Can. Geotech. J. 40 (2003) p.873.
[36] W.K. Leong, J. Chu and C.I. Teh, Geotech. Test. J. 23 (2000) p.178.
[37] L. Lancelot, I. Shahrour and M.A. Mahmoud, J. Eng. Mech. 130 (2004) p.1365.
[38] S. Sasitharan, P.K. Robertson, D.C. Sego and N.R. Morgenstern, Can. Geotech. J. 30 (1993) p.569.
[39] A. Gajo, L. Piffer and F. De Polo, Mech. Cohesive-Frictional Mater. 5 (2000) p.215.
[40] P. Cundall and O. Strack, Géotechnique 29 (1979) p.47.
[41] A. Tordesillas and M. Muthuswamy, J. Mech. Phys. Solids 57 (2009) p.706.
[42] D.M. Walker and A. Tordesillas, Int. J. Solids Struct. 47 (2010) p.624.
[43] A. Tordesillas, S. Pucilowski, D.M. Walker, J. Peters and M. Hopkins, Dynam. Continuous, Discrete Impulsive Syst., Ser. B 19 (2012) p.471.
[44] F. Radjai, D.E. Wolf, M. Jean and J.J. Moreau, Phys. Rev. Lett. 80 (1998) p.61.
[45] D.M. Walker, A. Tordesillas, R.P. Behringer, J. Zhang and J.F. Peters, Granular Matter 13 (2011) p.233.
[46] F. Darve and F. Laouafa, Mech. Cohesive-Frictional Mater. 5 (2000) p.627.
[47] F. Nicot and F. Darve, Int. J. Solids Struct. 44 (2007) p.6630.
[48] S. Lignon, F. Laouafa, P. Prunier, H.D.V. Khoa and F. Darve, Géotechnique 59 (2009) p.513.
[49] F. Nicot, F. Darve and H. Khoa, Int. J. Numer. Analyt. Meth. Geomech. 31 (2007) p.1007.
[50] J.F. Peters, M. Muthuswamy, J. Wibowo and A. Tordesillas, Phys. Rev. E 72 (2005) p.041307.
[51] F. Calvetti, G. Viggiani and C. Tamagnini, Rivista Italiana di Geotecn. 3 (2003) p.11.

[52] Y. Kishino, H. Akaizawa and K. Kaneko, *On the plastic flow of granular materials*, in *Powders and Grains*, Y. Kishino, ed., Zwets and Zeitlinger, Rotterdam, The Netherlands, 2001, p.199, ISBN: 9026518269.
[53] Y. Kishino, Rivista Italiana di Geotecn. 3 (2003) p.30.
[54] J. Bardet, Int. J. Plast. 10 (1994) p.879.
[55] F. Froiio and J. Roux, *Incremental response of a model granular material by stress probing with DEM simulations*, in in *Proceedings of the IUTAM-ISIMM Symposium on Mathematical Modeling and Physical Instances of Regular Flow*, J. Goddard, P. Giovine and J.T. Jenkins, eds., American Institute of Physics, Reggio Calabria, Italy, 2010, p.183.
[56] D.M. Walker, A. Tordesillas, I. Einav and M. Small, Phys. Rev. E 84 (2011) p.023101.
[57] H.P. Zhang, A. Be'er, E.L. Florin and H.L. Swinney, Proc. Nat. Acad. Sci. 107 (2010) p.13626.
[58] S.H. Strogatz, Nature 410 (2001) p.268.
[59] H. Jeong, B. Tombor, R. Albert, Z.N. Oltvai and A.L. Barabási, Lett. Nature 407 (2000) p.651.
[60] M.E.J. Newman, *Networks: An Introduction*, Oxford University Press, Oxford, 2010.
[61] S. Boccaletti, V. Latora, Y. Moreno, M. Chavez and D.U. Hwang, Phys. Rep. 424 (2006) p.175.
[62] L.D. Costa, F.A. Rodrigues, G. Travieso and P.R.V. Boas, Adv. Phys. 56 (2007) p.167.
[63] R.C. Arévalo, I. Zuriguel and D. Maza, Phys. Rev. E 81 (2010) p.041302.
[64] J.D. Horton, SIAM J. Comput. 16 (1987) p.385.
[65] K. Mehlhorn and D. Michail, ACM J. Exper. Algorithms 11 (2006) p.1.
[66] N. Rivier, *Granular matter with even circuits: Ball-bearings and dry quicksand*, in *Powders and Grains, Fifth International Conference on Micromechanics of Granular Media*, R. García-Rojo, H.J. Herrmann and S. McNamara, eds., Vol. 1, (Stuttgart, Germany), Balkema, The Netherlands, 2005, p.29.
[67] H.J. Herrmann, *Rotations in shear bands*, in *Trends in Computational Structural Mechanics*, W.A. Wall, K.-U. Bletzinger and K. Schweizerhof, eds., CIMNE, Barcelona, 2001, p.79.
[68] K. Bagi and M.R. Kuhn, J. Appl. Mech. 71 (2004) p.493.
[69] M. Muthuswamy and A. Tordesillas, J. Statist. Mech. (2006) p.P09003.
[70] C. Thornton and S.J. Antony, Powder Technol. 109 (2000) p.179.
[71] Z.P. Bažant and L. Cedolin, *Stability of Structures: Elastic, Inelastic, Fracture and Damage Theories*, Oxford University Press, New York, 1991.
[72] C. Thornton and S.J. Antony, Philos. Trans. R. Soc. London A 356 (1998) p.2763.
[73] N.P. Kruyt, C. R. Mec. 338 (2010) p.596.
[74] B.D. Ripley, J. R. Stat. Soc. Series B 39 (1977) p.172.
[75] P. Diggle, *Statistical Analysis of Spatial Point Patterns*, 2nd ed., Hodder Arnold, London, 2003.
[76] B.D. Ripley, *Spatial Statistics*, John Wiley, New York, 2005.
[77] A. Baddeley and R. Turner, J. Stat. Software 12 (2005) p.1.
[78] A. Getis and J. Franklin, Ecology 68 (1987) p.473.
[79] A. Baddeley, R. Moyeed, C. Howard and A. Boyde, Appl. Statist. 42 (1993) p.641.
[80] A. Tordesillas and M. Muthuswamy, Acta Geotech. 3 (2008) p.225.